

1
2
3
4
5
6
7
8
9
10
11
12
13
14
15
16
17
18
19
20
21
22
23
24
25
26

Gross Moist Stability and MJO Simulation Skill in Three Full-physics GCMs

James J. Benedict* and Eric D. Maloney

Department of Atmospheric Science, Colorado State University, Fort Collins, CO

Adam H. Sobel

Department of Applied Mathematics and Department of Earth and Environmental Sciences,

and Lamont-Doherty Earth Observatory

Columbia University, New York, NY

Dargan M. W. Frierson

Department of Atmospheric Sciences, University of Washington, Seattle, WA

Submitted to:

Journal of the Atmospheric Sciences

5 August 2013

* Current affiliation: Lawrence Berkeley National Lab, Berkeley, CA

Corresponding author address: James J. Benedict, Lawrence Berkeley National Lab, 1 Cyclotron Rd., MS 74-0171, Berkeley, CA 94720. E-mail: jjbenedict@lbl.gov

27 **Abstract**

28

29 Previous studies have demonstrated a link between gross moist stability (GMS) and intraseasonal
30 variability in theoretical and reduced-complexity models. In such simplified models, moisture modes—
31 convectively coupled tropical disturbances akin to the MJO whose formation and dynamics are linked to
32 moisture perturbations—develop only when GMS is either negative or “effectively” negative when
33 considering additional sources of moist entropy. These simplified models typically use a prescribed,
34 time-independent GMS value. Limited work has been done to assess GMS and its connection to
35 intraseasonal variability in full-physics general circulation models (GCMs).

36 The time-mean and intraseasonal behavior of normalized GMS (NGMS) are examined in three
37 pairs of GCMs to elucidate the possible importance of NGMS for the MJO. In each GCM pair, one
38 member produces weak intraseasonal variability while the other produces robust MJOs due to a change
39 in the treatment of deep convection. A highly correlated linear relationship between time-mean NGMS
40 and MJO simulation skill is observed, such that GCMs with less positive NGMS produce improved
41 MJO eastward propagation. The reduction in time-mean NGMS is primarily due to a sharp drop to
42 negative values in the NGMS component related to vertical advection, while the horizontal advection
43 component has a less clear relationship with MJO simulation. Intraseasonal fluctuations of anomalous
44 NGMS modulate the magnitude of background NGMS but generally do not change the sign of
45 background NGMS. NGMS declines ahead of peak MJO rainfall and increases during and after heaviest
46 precipitation. Total NGMS fluctuates during MJO passage but remains positive, suggesting that other
47 sources of moist entropy are required to generate an effectively negative NGMS.

48 **Section 1. Introduction**

49 The interaction between cumulus convection and the large-scale flow in which it is embedded is
50 a hallmark feature of many tropical weather systems, including the Madden-Julian Oscillation (MJO;
51 Madden and Julian 1971, Zhang 2005). Despite decades of advancement of conceptual theories,
52 enhanced modeling capabilities, and a greater scope and quality of tropical atmospheric measurements,
53 our understanding of such interactions remains incomplete. One approach to examining the relationship
54 between convective cloud systems and large-scale dynamics utilizes a concept called the gross moist
55 stability (GMS; Neelin and Held 1987). GMS quantifies the moist static energy or moist entropy export
56 in a convective overturning circulation per unit of mass transport. GMS provides a measure of the
57 efficiency with which convection and associated large-scale circulations discharge moist static energy or
58 moist entropy from the column, which in turn allows one to infer the strength of the circulation or
59 precipitation response to a given forcing in the column-integrated moist static energy budget. It emerges
60 naturally in any theory for tropical dynamics that focuses on the budget of moist static energy or moist
61 entropy, the most nearly conserved variables in a moist atmosphere.

62 In this study, we examine GMS in several pairs of general circulation models (GCMs) as a
63 means of diagnosing the role that GMS might play in determining the GCM's ability to realistically
64 simulate the MJO.

65 Observations of the tropical atmosphere indicate that the initiation and distribution of deep
66 convective precipitation is closely tied to the amount of moisture in the ambient lower and middle
67 troposphere (Sherwood 1999, Bretherton et al. 2004, Holloway and Neelin 2009). Cloud-resolving
68 model (CRM) studies suggest that this sensitivity arises from turbulent mixing between the cumulus
69 updrafts and environmental air through entrainment processes (Lucas et al. 2000, Derbyshire et al. 2004,
70 Raymond and Zeng 2005). The modulation of cumulus clouds by environmental humidity and the

71 feedbacks between convection and tropospheric moisture (among other factors, including radiation and
72 surface fluxes) have a critical impact on simulations of planetary-scale organized tropical convection in
73 reduced-complexity models (Bony and Emanuel 2005), CRMs (Hagos et al. 2011), and various types of
74 GCMs (Grabowski and Moncrieff 2004, Thayer-Calder and Randall 2007, Hannah and Maloney 2011).

75 One approach to understanding how tropical convection interacts with its environment is through
76 the use of simplified models. A diverse spectrum of simple theoretical models has been developed to
77 examine relationships among convection, moisture distribution, longwave radiation, and surface fluxes
78 (e.g., Emanuel et al. 1994, Neelin and Yu 1994; Neelin and Zeng 2000; Fuchs and Raymond 2002,
79 2005; Raymond and Fuchs 2007, 2009; Sugiyama 2009). Many theoretical studies focusing on such
80 interactions have implemented the weak temperature gradient (WTG) approximation, a simplified
81 dynamical framework that takes advantage of the spatial uniformity of temperature in the Tropics (e.g.,
82 Charney 1963; Held and Hoskins 1985; Sobel et al. 2001). Organized convective disturbances whose
83 development and dynamics are closely linked to moisture perturbations—so-called “moisture modes”—
84 become unstable in such models either when GMS is negative, or when “effective” GMS, including
85 radiative or surface flux feedbacks (Su and Neelin 2002, Bretherton and Sobel 2002, Sugiyama 2009,
86 Sobel and Maloney 2012, 2013) is negative.

87 GMS is broadly defined as the ratio of vertically integrated horizontal divergence of an intensive
88 quantity conserved under moist adiabatic processes to some measure of convective intensity. In this
89 study we use specific moist entropy s as the conserved quantity following Raymond et al. (2010) and
90 references therein. A version of GMS, the “normalized” GMS (or NGMS), is derived from the budget
91 of vertically integrated s and may be written as

$$\Gamma_T = -\frac{T_R[\nabla \cdot (s\mathbf{v})]}{L[\nabla \cdot (r\mathbf{v})]}, \quad (1)$$

92 where $T_R = 273.1\text{K}$, $L = 2.5 \times 10^6 \text{ J kg}^{-1}$, r is the water vapor mixing ratio, \mathbf{v} is the horizontal vector
93 wind, and $[\cdot]$ represents a mass-weighted vertical integral from the surface to the tropopause. Note that
94 we use vertically integrated moisture convergence as the normalization factor in (1), as opposed to the
95 dry static energy export that is used in some other studies (e.g., Wang and Sobel 2011, 2012; Sobel and
96 Maloney 2012, 2013); results are not expected to be particularly sensitive to this choice. Another
97 difference of convention is that the definition of GMS here is based on the total horizontal flux
98 divergence, which includes horizontal advective tendencies, whereas in some studies the GMS refers
99 only to what is called here the “vertical component” (see Eqs. 3-5) with horizontal advection treated as
100 external.

101 In steady state conditions, we can formulate an expression demonstrating the sensitivity of net
102 precipitation to NGMS as $P = E + T_R(F_S - R)/L\Gamma_T$. Here, P and E are time-mean precipitation and
103 evaporation, respectively; F_S is the surface entropy flux; and R is the column entropy sink due to
104 radiative cooling. The expression indicates that precipitation, at least in the time mean, becomes a
105 stronger function of entropy forcing ($F_S - R$) if NGMS is small. The entropy forcing increases when F_S
106 increases due to larger surface evaporative or sensible heat fluxes, or when R decreases due to reduced
107 longwave cooling to space in the presence of abundant upper-level cloudiness and moisture.

108 If we don't assume steady state, but we do assume that free tropospheric temperature variations
109 are small, then the sign of the NGMS tells us how convection feeds back onto the moisture field
110 (Raymond 2000). If the NGMS is negative, convection strong enough to drive large-scale ascent results
111 in an increase in column moist static energy, thus promoting an environment favorable for future
112 convection. If the NGMS is positive, the convection and large-scale ascent dry the environment despite
113 moisture convergence. As a simple example, we highlight the link between cloud characteristics and the
114 NGMS vertical component (see Eq. 5): we associate negative NGMS with shallow convective or

115 congestus cloud regimes and a net import of column s , while positive NGMS is characterized by more
116 mature convection and cumulonimbi-driven stratiform clouds that produce a net export of column s . An
117 informative review of GMS can be found in Raymond et al. (2009).

118 In order for the GMS to be part of a successful theory for tropical precipitation, we need a theory
119 for the value of the GMS itself as a function of environmental conditions. The observational study of
120 López Carillo and Raymond (2005) indicates that GMS is a function of saturation fraction, in which
121 drier regimes have lower column moisture and import s ($GMS < 0$) while regimes with higher column
122 moisture export s ($GMS > 0$). Consistent with this, single-column models (SCMs) and CRMs run in
123 WTG mode can produce two stable equilibria for the same boundary conditions and forcings. One
124 corresponds to dry conditions and has $GMS < 0$; this still implies export of moist static energy, but
125 associated with a descending large-scale circulation. The other corresponds to wet conditions and has
126 $GMS > 0$ (Sobel et al. 2007, Sessions et al. 2010). These SCM and CRM results are consistent with
127 those of Bretherton et al. (2005), who noted self-aggregating convective clusters produced in an
128 idealized CRM in radiative-convective equilibrium (RCE) on a large domain. The clusters and dry
129 regimes within the large domain are thought to correspond to the wet and dry regimes in the smaller-
130 domain simulations under WTG (although the correspondence cannot be exact because, in RCE, the dry
131 and wet regimes cannot both export moist static energy, as they can in the WTG solutions, because the
132 net export of moist static energy from a domain in RCE must vanish). Though simplistic, these results
133 form the foundation of our view of the cyclic convectively suppressed and active phases observed in
134 large-scale tropical disturbances such as the MJO.

135 In many reduced-complexity models, moisture modes become destabilized if NGMS is negative
136 (e.g., Sobel et al. 2001; Raymond and Fuchs 2007, 2009; Sugiyama 2009). Favorable conditions for
137 moisture mode instability can also be achieved even if NGMS, as defined in (1), is positive given the

138 presence of other diabatic processes that increase column moist entropy, such as surface fluxes and
139 radiation (e.g., Sugiyama 2009; Sobel and Maloney 2012, 2013).

140 While the GMS plays a key role in many idealized models of tropical dynamics, the GMS is
141 particularly sensitive to the assumptions of vertical structure that are made, implicitly or explicitly, in
142 those models (e.g., Sobel et al. 2007). Many reduced-complexity modeling studies of moisture modes
143 (Neelin and Yu 1994, Fuchs and Raymond 2005, Raymond and Fuchs 2009, Sugiyama 2009) explicitly
144 assume a pure first baroclinic mode (deep convective) structure, even though many tropical
145 disturbances, including the MJO, project significantly on second baroclinic mode structures, and the
146 second mode plays an important dynamical role in some theories for these disturbances (e.g., Mapes
147 2000, Madja et al. 2004, Khouider and Majda 2006, Kuang 2008). Some idealized models allow for
148 multiple vertical modes and determine the GMS interactively; Kuang (2011) argues that feedbacks
149 between the temperature field and the GMS are important to MJO dynamics. A few studies have
150 analyzed the GMS in CRM studies either with an explicit large-scale circulation (Kuang 2012) or with
151 parameterized large-scale dynamics (Raymond and Sessions 2007; Sessions et al. 2010; Wang and Sobel
152 2011, 2012); either choice allows a full range of variation in vertical structure, rather than a small
153 number of vertical modes as in more idealized models. Frierson (2007) diagnosed the GMS in an
154 idealized GCM with several different convective parameterizations and found it to be a useful diagnostic
155 for understanding the dependence of the general circulation on the choice of parameterization.

156 In this study, we analyze the behavior of GMS in three pairs of full-physics GCMs, and focus on
157 the relationship between the GMS and the simulated intraseasonal variability. In each pair of GCMs,
158 one member produces weak intraseasonal variability while its counterpart produces stronger
159 intraseasonal variability and more realistic MJO disturbances due to a change in the treatment of deep
160 convection. Our goal is to investigate what role, if any, GMS plays in explaining the differences seen

161 within each GCM pair. Our analysis will examine both the time-mean GMS and its intraseasonal
162 fluctuations. Hannah and Maloney (2011) analyzed a series of GCM simulations in a single model and
163 found a reduction in time-mean GMS when minimum cumulus entrainment and rain evaporation were
164 increased to produce stronger MJO activity. Intraseasonal variability in GMS was also increased with
165 such modifications. Additionally, Frierson et al. (2011) ascribed the slower propagation of convectively
166 coupled Kelvin waves in a suite of GCMs with modified convective parameterizations to reduced time-
167 mean GMS. As suggested by Raymond et al. (2009), the assessment of GMS in simulations with
168 different cumulus parameterization schemes may help us understand model weaknesses by highlighting
169 processes that are unrealistically suppressed or overemphasized.

170 A description of the data sources and a review of the model simulations are presented in Section
171 2. We provide a commentary on the calculation of GMS in Section 3. Our primary findings are
172 presented in Section 4, followed by a discussion of the results and concluding remarks in Section 5.

173

174 **Section 2. Data and Model Description**

175 We investigate the behavior of GMS and related variables in three pairs of GCMs, resulting in a
176 total of six simulations. In each GCM pair, one model version produces weak tropical intraseasonal
177 variability (the “control” simulation) while the other member produces stronger intraseasonal variability
178 due to a modification in the treatment of deep convection (the “modified” simulation). Table 1 lists the
179 GCM simulations examined in this study and other salient information related to their treatments of deep
180 convection.

181 The first GCM pair consists of two versions of the GFDL AM2 (Anderson et al. 2004). Both
182 versions of the AM2 parameterize cumulus convection using the relaxed Arakawa-Schubert (RAS;
183 Moorthi and Suarez 1992) scheme consisting of a spectrum of entraining plumes. Also included is a

184 modification that suppresses deep convective updrafts with lateral entrainment rates below a minimum
185 threshold $\mu_{min} = \alpha/D$, where α is a positive constant and D is the subcloud layer depth (Tokioka et al.
186 1988). Consistent with previous studies (Hannah and Maloney 2011, Kim et al. 2011), increasing the
187 value of α in AM2-TOK results in stronger intraseasonal variability (see Section 4).

188 The second GCM pair consists of two versions of the GFDL AM3 (Donner et al. 2011). Many
189 features of AM3 differ greatly from the AM2, including the dynamical core, spatial grid, and treatment
190 of deep and shallow convection (see Donner et al. 2011 or Benedict et al. 2013 for further details). The
191 deep convection scheme includes parameterizations for both deep cumulus plumes and, unlike in AM2,
192 dynamically active mesoscale anvil clouds that modulate local radiative fluxes and water substance
193 transport between the cumuli and their environment. In AM3-CTL, the convective closure assumption
194 is based on relaxing CAPE back to a reference value over a specified time scale, activation of deep
195 cumuli is prohibited if convective inhibition (CIN) is greater than 100 J kg^{-1} or CAPE is less than 1000 J
196 kg^{-1} , and convective downdrafts are not parameterized. In the modified AM3 (AM3-A), the default
197 CAPE relaxation closure is replaced by the Zhang (2002) closure. The CAPE and CIN thresholds that
198 restrict deep convective initiation are supplemented with an additional convective trigger that requires
199 time-integrated low-level parcel ascent to exceed a specified magnitude for deep cumuli to form
200 (Donner et al. 2001). Although neglected in AM3-CTL, convective downdrafts are parameterized in
201 AM3-A and so we expect stronger interactions between convection and environmental moisture. The
202 modifications to the treatment of deep convection in the AM3 result in stronger intraseasonal variability
203 at the expense of a degraded mean state (see Fig. 1).

204 The final GCM pair consists of version 3.0 of the standard NCAR Community Atmosphere
205 Model (CAM; Collins et al. 2006) and its superparameterized (SP) variant, the SPCAM (Khairoutdinov
206 et al. 2008, hereafter KDR08). Both simulations are run using a semi-Lagrangian dynamical core at

207 2.8°×2.8° horizontal resolution (T42 spectral truncation). The Zhang-McFarlane (1995) deep
208 convection scheme employed by CAM3.0 accounts for convective downdrafts and assumes that CAPE
209 is consumed by cumuli at a specified rate. CAM3 acts as the host GCM for the SPCAM simulation.
210 Using the SP approach, a 2D north-south-oriented “curtain” CRM with 32 columns, 28 levels collocated
211 with the lowest 28 CAM levels, and 4 km horizontal resolution is embedded into each CAM grid cell.
212 The embedded CRMs replace CAM’s conventional parameterizations of convection and boundary layer
213 processes. Additional background information of the SPCAM simulation examined in this study and the
214 SP approach can be found in KDR08 and Benedict and Randall (2009). Compared to the standard
215 CAM3, notably stronger intraseasonal variability is observed in CAM simulations that utilize the SP
216 approach (KDR08, Benedict and Randall 2009).

217 All AM simulations are run for 11 years, with the first year discarded to mitigate the effects of
218 model spin-up. Lower boundary forcing consists of the climatological (1981 to ~2000) mean seasonal
219 cycle at monthly temporal resolution of SSTs and sea ice concentrations taken from Reynolds et al.
220 (2002) for AM2 and Hurrell et al. (2008) for AM3. The CAM/SPCAM simulations span 19 years
221 (1985-2004) and use observed monthly SSTs and sea ice concentrations (Hurrell et al. 2008), but only
222 data between 1986-2003 is presented in this study.

223 The six GCM simulations are compared to satellite-based precipitation estimates and reanalysis
224 data products. For simple climatological comparison (Fig. 1 only), the simulations are validated against
225 1980-2000 mean rainfall from Global Precipitation Climatology Project (GPCP; Adler et al. 2003) and
226 mean 850 hPa zonal winds from the ECMWF-Interim reanalysis (hereafter, ERAI; Berrisford et al.
227 2009). For all other figures, precipitation from the Tropical Rainfall Measuring Mission (TRMM) 3B42
228 version 6 data product (Huffman et al. 2007) and dynamic and thermodynamic variables from ERAI

229 during the 1999-2008 period are used to validate the simulations¹. Differences between the TRMM
 230 3B42 and GPCP rainfall products are insignificant for our purposes (Kim et al. 2013a). Although
 231 mostly offset from the simulation time spans, we chose to use the 1999-2008 validation period because
 232 satellite-based estimates of precipitation at daily resolution are only available after late 1997. In this
 233 paper we will refer to the validation data sets as “observations,” but some amount of caution is advised.
 234 Few “ground truth” meteorological stations exist over the open Indian and West Pacific Ocean regions
 235 where the MJO is most active, limiting the rain gauge data that is streamed into the TRMM 3B42
 236 product and forcing ERAI to be more strongly constrained by model parameterizations (rather than
 237 radiosondes) in these areas. All model and validation data are daily averaged and linearly interpolated
 238 to the 27 ERAI standard pressure levels and a 2.5° horizontal grid.

239

240 **Section 3. Calculation of Moist Entropy and GMS**

241 A number of calculations and assumptions are needed to obtain the advective components that
 242 make up the GMS. As mentioned in Section 1, our version of GMS uses specific moist entropy s as the
 243 variable that is conserved under moist adiabatic processes. We use the following equation for s , which
 244 is valid for temperatures either above or below freezing (Raymond 2013):

$$s = (C_{PD} + r_V C_{PV}) \ln(T/T_R) - R_D \ln(p_D/p_R) - r_V R_V \ln(p_V/e_{SF}) + (L_V r_V/T_R) \quad (2)$$

245 In (2), the specific heat, gas constant, and partial pressure of dry air are C_{PD} , R_D , and p_D , respectively;
 246 the specific heat, gas constant, and partial pressure of water vapor are C_{PV} , R_V , and p_V , respectively; r_V is
 247 the water vapor mixing ratio; T is air temperature; $T_R = 273.1\text{K}$; $e_{SF} = 611\text{ Pa}$; and $L_V(T) \approx$
 248 $2.5 \times 10^6\text{ J kg}^{-1}$ is the enthalpy of vaporization. Liquid water and ice mixing ratios do not appear in (2)

¹ For moist entropy budget plots shown in Fig. 10, surface latent heat fluxes are taken from the objectively analyzed surface flux data set as described in Yu and Weller (2007).

249 because they were not written to the AM daily output files. However, we found that liquid and ice only
 250 weakly influence s .

251 Following Raymond et al. (2007) and Raymond et al. (2009), we define the total, horizontal, and
 252 vertical advective components of the NGMS as:

$$\Gamma_T = -\frac{T_R[\mathbf{v} \cdot \nabla s + \omega(\partial s / \partial p)]}{L[\nabla \cdot (r\mathbf{v})]} \quad (3)$$

$$\Gamma_H = -\frac{T_R[\mathbf{v} \cdot \nabla s]}{L[\nabla \cdot (r\mathbf{v})]} \quad (4)$$

$$\Gamma_V = -\frac{T_R[\omega(\partial s / \partial p)]}{L[\nabla \cdot (r\mathbf{v})]} \quad (5)$$

253 In (3)-(5), $[\cdot]$ represents a mass-weighted vertical integral from the surface to 100 hPa, \mathbf{v} is the
 254 horizontal vector wind, ω the vertical pressure velocity, $L = 2.5 \times 10^6 \text{ J kg}^{-1}$ (simplified to be
 255 temperature-independent due to the column integral), r the water vapor mixing ratio, and ∇ the gradient
 256 operator on a constant-pressure surface. We again neglect the presence of liquid and ice. All spatial
 257 derivatives are computed before interpolation to a unified $2.5^\circ/27$ -level grid, and when calculating
 258 horizontal derivatives we account for small horizontal pressure changes along a given level of the model
 259 hybrid coordinate. We elect to use the advective form of Γ_T (Eq. 3) rather than its flux form, $\Gamma_T =$
 260 $-\frac{T_R[\nabla \cdot (s\mathbf{v})]}{L[\nabla \cdot (r\mathbf{v})]}$. Arakawa et al. (2004) demonstrate that budget considerations of intensive quantities such as
 261 s are best characterized using the advective form rather than the flux form of the advection equation.

262 To generate a statistically stable quantity, substantial space-time averaging of terms that
 263 comprise (3)-(5) is required. Following the methods outlined in Raymond et al. (2009), we first average
 264 the numerator and denominator separately and then combine them to obtain NGMS. For time-mean
 265 plots of NGMS (see Figs. 4 and 5), we spatially average the data using a 7.5° sliding-box smoothing
 266 centered at each grid point. No land points are included in the averaging. For NGMS calculations that

267 do not involve taking climatological means (e.g., Fig. 9), we apply a 17-day running average and 12.5°
268 sliding-box smoothing to both numerator and denominator separately. Of several space-time smoothing
269 approaches tested, this one yielded a satisfying compromise between statistical stability and preservation
270 of MJO-scale features. NGMS values are discarded wherever vertically integrated moisture
271 convergence is less than $|5| \text{ W m}^{-2}$ to avoid division by zero. The basic features discussed in Sec. 4 are
272 not sensitive to reasonably small changes in this smoothing approach.

273 Several issues arise regarding our choice of the total and vertical components of column-
274 integrated s advection and the potential sources of error in our computations of these quantities. First,
275 all advection calculations are made on post-processed data and not online within the model integration
276 itself. This may introduce errors due to space-time interpolation and averaging. For example, AM3
277 output is first daily averaged and interpolated from the native cubed-sphere grid to a latitude-longitude
278 grid prior to calculation of advection. Additionally, large differences between CAM advection terms
279 computed during integration using spherical harmonics and those computed during post-processing are
280 known to exist. Ideally, advection terms should be computed during model integration. Second, a
281 strong sensitivity to the chosen limits of column integration exists. Deep convective areas typically have
282 a large convergence of s near the surface and a slightly larger divergence of s near the tropopause,
283 indicating that vertically integrated advection may be a residual of two large terms. Third, ω is small
284 but not zero at the top and bottom of our chosen atmospheric column (surface and 100 hPa,
285 respectively), while we do assume $\omega = 0$ when formulating the vertical integrals of either the flux or
286 advective forms of s advection. These three issues contribute to non-negligible differences between the
287 flux and advective forms of Γ_T . Over the Indo-Pacific, the temporal correlations between these two
288 forms range from 0.3 in CAM to >0.9 in AM2 (both values are statistically significant above the 99%

289 level), but the corresponding local root-mean-square differences can exceed the local standard deviation
290 indicating that in some instances the errors may be large compared to typical magnitude fluctuations.

291

292 **Section 4. Results**

293 Figure 1 shows (a) October-April (hereafter, “winter”) mean precipitation and 850-hPa zonal
294 winds (hereafter, “U850”) based on GPCP and ERAI, respectively, and (b-g) the winter-mean
295 precipitation differences (model–GPCP) and the mean U850 for each simulation. Details of the
296 simulation biases are reported in other studies (Benedict and Randall 2007, Benedict et al. 2013), but
297 here we briefly highlight features most relevant to the MJO. Despite very different deep convective
298 parameterizations, the changes seen in U850 between the control and modified simulations are
299 surprisingly consistent among the GCM pairs. In each control run, the strip of equatorial U850
300 westerlies in the Indian Ocean is realistic but its eastward extension is too limited compared to
301 observations. All modified simulations—those producing an improved MJO—display weakened
302 westerlies in the Indian Ocean, while AM2-TOK and SPCAM display a tendency to extend the
303 westerlies further into the West Pacific, as is seen in reanalysis. Each simulation generally
304 overestimates Indo-Pacific rainfall, particularly in the west and northeast Indian Ocean and along the
305 climatological convergence zones in the Pacific. With the exception of AM3-CTL, all simulations also
306 underestimate rainfall in the east Indian Ocean just south of the Equator where the MJO is most active
307 (Salby and Hendon 1994, Wheeler and Kiladis 1999, Sobel et al. 2010). Numerous studies have
308 demonstrated that an important link exists between the mean state and the MJO in GCM simulations
309 (Inness et al. 2003, Zhang et al. 2006, Kim et al. 2011).

310 Raw spectral power of the equatorially symmetric component of tropical rainfall is displayed in
311 Fig. 2. These plots are made using the methodology of Wheeler and Kiladis (1999) and are adapted

312 from Fig. 6 in Benedict et al. (2013) with the addition of the results for the CAM and SPCAM. Note
313 that for all of our analyses of intraseasonal disturbances (all remaining figures) we analyze TRMM
314 rather than GPCP rainfall, as discussed in Sec. 2.

315 Fig. 2 shows that our modifications to the treatment of deep convection (as well as other
316 processes, for the SPCAM) uniformly enhance low-frequency variability but, more importantly, improve
317 the distribution of spectral power by shifting the peak from westward- to eastward-propagating
318 disturbances. AM2-TOK overestimates power in the MJO spectral range (here, defined as zonal
319 wavenumbers +1 to +3 and periods of 30-96 d) but produces only extremely weak Kelvin waves (Fig.
320 2c). MJO power is more realistic in AM3-A (Fig. 2e) but it is at a higher frequency (~30 d) than in
321 observations (~45 d) and is not easily distinguishable from power associated with low-frequency Kelvin
322 waves. SPCAM generates a realistic distribution of rainfall spectral power associated with both the
323 MJO and Kelvin waves (Fig. 2g), as shown in previous studies (Khairoutdinov et al. 2005, Benedict and
324 Randall 2007). Of the modified GCMs examined here, the spectral pattern of eastward-moving tropical
325 disturbances is best depicted by SPCAM while AM2-TOK struggles to produce convectively coupled
326 Kelvin waves.

327 Lag correlation plots presented in Fig. 3 provide added insight into the space-time relationships
328 between convective forcing and the dynamical response of the simulated MJO. In Fig. 3, we lag-
329 correlate U850 with an index timeseries of equatorial rainfall based at either 90°E (left) or 150°E (right).
330 For all variables, anomalies as defined by the departure from the calendar-day mean are 20-100-day
331 bandpass filtered prior to correlation. Following the spectral distributions of Fig. 2, all control
332 simulations produce disturbances that are highly inconsistent with observations (Figs. 3a,b). Although a
333 well-defined signal moving eastward at the correct speed is noted in the West Pacific in AM2-TOK (Fig.
334 3f), this model only produces a weak and localized disturbance in the east Indian Ocean without clear

335 eastward movement (Fig. 3e). Compared to AM2-TOK, AM3-A depicts a stronger and more coherent
336 MJO signal in both ocean basins, but the simulated MJO phase speed is too fast in the west Pacific
337 (Benedict et al. 2013). The apparent signal of westward-moving equatorial Rossby waves in the Indian
338 Ocean is overemphasized in AM3-A compared to observations. SPCAM is able to reproduce observed
339 MJO phase speeds in both ocean basins, but correlations are lower than those seen in nature. Our
340 overall impression from Figs. 2 and 3 is that, compared to observations, all modified GCMs simulate the
341 MJO reasonably well in the west Pacific. In the Indian Ocean only AM3-A and SPCAM are able to
342 simulate the MJO's eastward propagation to any degree, but even those have significantly weaker
343 correlations than do the observations.

344 In Fig. 4 we present, from top to bottom, winter means of the horizontal ($T_R[\mathbf{v} \cdot \nabla s]$), vertical
345 ($T_R[\omega(\partial s / \partial p)]$), and total ($T_R[\mathbf{v} \cdot \nabla s + \omega(\partial s / \partial p)]$) components of moist entropy export derived from
346 ERAI. In each panel, thin and thick black lines represent the 3 and 6 mm d⁻¹ precipitation contours,
347 respectively. Horizontal advection exports column moist entropy [s] (Fig. 4a) for all rainy regions of the
348 tropical Indo-Pacific region. Vertical advection tends to weakly export [s] where mean Indo-Pacific
349 rainfall is greatest, from the eastern Indian Ocean to the SPCZ in the West Pacific. An import of [s] by
350 vertical circulations is seen along the central-eastern Pacific ITCZ. Overall, [s] export is strong and
351 dominated by horizontal advection in the Indo-Pacific warm pool but near zero along the eastern Pacific
352 ITCZ due to a counteracting import by vertical circulations. Previous studies have examined annual
353 mean, column-integrated moist static energy export using a variety of reanalysis data sources (with
354 different moist physics parameterizations), spatial grids, and analysis techniques (e.g., Back and
355 Bretherton 2006, Peters et al. 2008). Our annual mean [s] export plots (not shown) are consistent with
356 those reported previously and give us confidence that the results of Fig. 4 are reasonably accurate.

357 A comparison of winter-mean and meridionally averaged terms related to NGMS is shown in
358 Fig. 5. Meridional averaging is computed using a dynamic latitude mask that includes only oceanic grid
359 points where winter-mean vertically integrated moisture convergence (VIMC) is positive. We restrict
360 the latitudinal bounds to be at most 15° from the Equator. This meridional bounding is approximated by
361 the 3 mm d^{-1} contour of mean rainfall and effectively defines areas in each data set where climatological
362 deep convection occurs. Our results are not sensitive to whether we choose to use a fixed (e.g., 15°S -
363 10°N) or dynamic latitude range. In Fig. 5, two passes of a 1-2-1 filter have been applied in longitude
364 prior to plotting. Compared to their corresponding control GCM simulations (dashed lines), each
365 modified simulation (solid gray lines) produces a stronger winter-mean $[s]$ export by horizontal
366 circulations (top row) but consistently stronger $[s]$ import (or weaker $[s]$ export) by vertical circulations
367 (second row). Total $[s]$ export (third row) in the modified simulations—those with stronger MJOs—
368 may be either stronger or weaker than total $[s]$ export in the control runs depending whether the
369 horizontal or vertical exports are dominant.

370 As discussed in Sec. 3, moisture modes can develop in reduced-complexity GCMs when
371 normalized GMS (“NGMS”) is either negative or effectively negative when cloud-radiative and surface
372 flux feedbacks are included. Longitudinal profiles of the winter-mean horizontal, vertical, and total
373 components of NGMS (rows 4-6, denoted by Γ_H , Γ_V , and Γ_T in Fig. 5, respectively) reveal a consistent
374 theme for all models: compared to their respective control runs, a reduction in Γ_T seen in each modified
375 simulation (dashed black) is driven exclusively by a strong reduction in Γ_V , while Γ_H values in the
376 modified simulations are similar to or slightly higher than those in the control runs (solid gray).
377 Strongly reduced magnitudes of Γ_V and Γ_T occur for all longitudes even in the presence of a diverse
378 distribution of column-integrated moisture convergence ($-L[\nabla \cdot (r\mathbf{v})]$; second row from bottom) that in
379 the modified simulations may be stronger (e.g., in the west Pacific) or weaker (e.g., near the Maritime

380 Continent) than their respective control runs. These smaller positive values of Γ_T seen in each modified
381 simulation increase the sensitivity of time-mean precipitation to a given entropy forcing, as in (1).
382 Figure 5 clearly suggests that changes made to the treatment of deep convection that improve MJO
383 strength in the three GCMs analyzed are closely linked to the behavior of time-mean NGMS in those
384 models, and that for each model these deep convective parameterization changes resulted in a strong
385 reduction in Γ_T that is driven exclusively by strong negative tendencies in Γ_V .

386 The relationship between winter-mean Γ_V and one measure of the robustness of MJO eastward
387 propagation is shown in Fig. 6. The Γ_V values represent spatial averages within the climatological deep
388 convection region (50°E to 150°W and within a dynamic latitude range to include only oceanic grid
389 points where winter-mean VIMC is positive; see previous discussion on dynamic latitude range). The
390 MJO metric used here is nearly identical to the level-2 diagnostic from CLIVAR MJO Working Group
391 (2009) and Kim et al. (2009) and is defined as the ratio of east-to-west raw spectral power of tropical
392 rainfall, where eastward signals represent the sum of power within the MJO spectral region of zonal
393 wavenumbers +1 to +3 and periods 30-96 d while their westward counterparts are bounded by zonal
394 wavenumbers -1 to -3 in the same range of periods. Figure 6 shows a coherent linear relationship
395 between Γ_V and the MJO metric in which each simulation that produces a better MJO has both a more
396 negative Γ_V value and a more positive east-west ratio. A similar relationship between the MJO metric
397 and Γ_T is noted (slope $m = -2.9$, $r = -0.92$; plot not shown), although the linear pattern shifts to
398 higher Γ_T values where modified simulations loosely cluster around +0.17 while control simulations
399 cluster around +0.32. No clear relationship exists between the MJO metric and Γ_H , ($m = +1.9$, $r =$
400 +0.41). This suggests that the vertical rather than the horizontal time-mean NGMS component is more
401 closely tied to total NGMS variations and appears to play a more significant role in determining the
402 model's ability to realistically simulate the MJO. Figure 6 is an exercise in understanding possible

403 connections between NGMS and the MJO in the GCM simulations, and so we omitted the point based
404 on ERAI. The location of the reanalysis point ($\Gamma_V = +0.01$, E-W ratio = +2.4) falls well off the best-
405 fit line and suggests that, acknowledging the uncertainties of the reanalysis data set, some deficiencies in
406 the simulated relationship between deep convection and the large-scale circulation remain. Factors other
407 than time-mean GMS such as rain intensity-dependent moisture distributions may also affect the MJO
408 (Kim et al. 2013b).

409 Figures 5 and 6 show associations between winter-mean NGMS and the MJO in the GCM pairs.
410 We now examine how NGMS varies as a function of convective activity, with implications for NGMS
411 variations during MJO events. Figure 7 shows scatterplots of the vertical ($T_R[\omega(\partial s/\partial p)]$) and horizontal
412 ($T_R[\mathbf{v} \cdot \nabla s]$) components of moist entropy divergence versus VIMC ($-L[\nabla \cdot (r\mathbf{v})]$). Each dot represents
413 a daily value over the east Indian Ocean (70°-100°E, 10°S-5°N), but we reiterate that a sliding 17-day
414 window smoothing is applied to compute the components. Scatterplots using equatorial West Pacific
415 data (omitted) are qualitatively similar to Fig. 7. The results for ERAI indicate that horizontal advection
416 nearly always works to reduce column s in moist regions regardless of the sign or magnitude of VIMC.
417 However, vertical advection is significantly correlated with VIMC such that s divergence due to vertical
418 advection increases with increasing VIMC. Conversely, when convective intensity is weaker (i.e.,
419 negative or weakly positive VIMC), vertical advection can contribute to convergence of s into the
420 column. We hypothesize that the behavior seen in the ERAI vertical advection component may be
421 related to cloud regime fluctuations on subseasonal scales. Presumably, strongly positive VIMC
422 represents regions of mature cumulonimbi and their associated abundant stratus clouds that are effective
423 at reducing column s . Weakly positive VIMC likely represents areas of shallow cumuli or congesti,
424 whose circulations can increase column s as noted in Fig. 7, consistent with previous observational
425 analyses (e.g. Haertel et al. 2008). Further discussion on this topic appears in Sec. 5.

426 Each control simulation—one that produces unrealistically weak intraseasonal variability—
427 qualitatively reproduces the general relationship between s divergence and VIMC (Fig. 7, left).
428 Strikingly different behavior is noted in the simulations that have more intense MJOs (Fig. 7, right). In
429 both AM modified runs, horizontal advection is a strongly increasing function of VIMC and, as in the
430 ERAI panel, exports s from the column. Vertical advection is a decreasing function of VIMC and is
431 mostly involved in s import. Thus, when VIMC is strongly positive in the presence of vigorous deep
432 convection, vertical circulations still converge s into the column while horizontal advection does all of
433 the “heavy lifting” to export the excess s . We note that vertical advection in the West Pacific (not
434 shown) shows a greater tendency for s divergence but is insensitive to VIMC for AM2-TOK and AM3-
435 A. Interestingly, SPCAM is better able to reproduce the key advective features seen in the ERAI plot,
436 including the positive slope of the vertical advection-VIMC line. The toy model of Raymond and Fuchs
437 (2009), which produces robust MJO-like disturbances, depicts relationships between s divergence and
438 VIMC that are very similar to the results for AM2-TOK and AM3-A, while the results of SPCAM are
439 closer in line with ERAI.

440 The fact that the AM2-CTL and AM3-CTL (and possibly CAM) distributions of entropy
441 divergence versus convective activity more resemble ERAI than those from the perturbed model
442 versions with stronger MJO is interesting. We propose two possibilities to explain this dilemma. One
443 possibility is that the ERAI advective tendencies are in error due to missing or incorrect physics in the
444 reanalysis model. While we do not have access to ERAI analysis increments that are generated in the
445 process of data assimilation to reconcile the model state with observations, previous work with
446 reanalysis datasets indicates that such analysis increments may be large in the context of MJO heat and
447 moisture budgets. For example, Mapes and Bacmeister (2012) demonstrate that the Modern-Era
448 Reanalysis for Research and Applications has a large positive moisture budget analysis increment in the

449 shallow convective phase of the MJO, suggesting a lack of deep convective restraint, which would also
450 suggest that NGMS is too high during this period. Kiranmayi and Maloney (2011) also note a large
451 positive residual in the moist static energy budget during the moistening phase of the MJO lifecycle in
452 ERAI fields. Moist static energy advective tendencies in this study were calculated using standard model
453 output variables and analysis increments were not available. Another possibility to explain differences
454 between ERAI and model entropy budgets is that AM3-A and AM2-TOK may be producing more
455 realistic MJO variability for the wrong reasons. Figure 7 suggests that even for high precipitation rates,
456 divergent circulations are importing moist entropy into the column in these models. Horizontal
457 advection must compensate to maintain energy balance, which is reflected in a greater slope for
458 horizontal entropy divergence in AM3-A and AM2-TOK relative to the control versions of these
459 models. Kim et al. (2011) demonstrated that models with stronger intraseasonal variability often have
460 common mean state biases, such as excessive mean precipitation in the off-equatorial west Pacific
461 during boreal summer. These biases might reflect the need for the models to accomplish more energy
462 transport to high latitudes by the rotational flow to compensate for unrealistic vertical advection.

463 Figures 5-7 suggest that vertical advection plays an important role for the MJO on time-mean
464 scales and as convective intensity fluctuates by importing column-integrated s during periods of
465 relatively weak moisture convergence. Given that VIMC is on average positive in the MJO active
466 regions even during its suppressed phase (not shown), (5) indicates that the sign of Γ_V is determined by
467 $[\omega(\partial s / \partial p)]$. Profiles of s and normalized vertical pressure velocity $-\omega$ show the connections between
468 NGMS, s import, and the cloud regimes observed during different phases of the MJO. In Fig. 8 we
469 display profiles of s and $-\omega$ averaged over the equatorial east Indian Ocean region (85°-95°E) only
470 during MJO suppressed conditions between October and April. We define the suppressed phase as
471 winter days when 20-100-day filtered and standardized east Indian Ocean rainfall is less than -1σ .

472 Because this threshold captures some lightly raining situations, the $-\omega$ profiles are weakly positive and
473 this behavior is magnified by the normalization. Profiles for the convectively active phase are omitted
474 because, for all data sources, $-\omega$ shows a “top-heavy” profile with a maximum near 350 hPa, the
475 minimum in s occurs at a much lower level ($\sim 600-750$ hPa), and therefore vertical circulations
476 effectively export s out of the column [see Sec. 4.4 in Raymond et al. (2009) or Sec. 5 of this paper for
477 further discussion]. Larger differences among the simulations are noted during the MJO suppressed
478 phase. The AM2 s and $-\omega$ profiles are similar to AM3 and so are omitted in Fig. 8. Qualitatively
479 similar s profiles are seen among the AM3 profiles, but AM3-A produces a more realistic lower- to mid-
480 tropospheric peak in $-\omega$ (Fig 8b). For AM3-A, $-\omega$ is larger where $\partial s / \partial p$ is positive and smaller where
481 $\partial s / \partial p$ is negative, yielding negative Γ_V and thus s import. In AM3-CTL, however, $-\omega$ is weighted more
482 heavily toward the upper troposphere and exhibits a peak well above the minimum in s (Fig. 8a),
483 resulting in positive Γ_V and s export. Slightly different behavior is noted in the CAM-SPCAM
484 comparison, although the end result is the same. Although the CAM $-\omega$ maximum matches ERAI (Fig.
485 8d), its s minimum occurs at a much lower pressure level (Fig. 8c). Thus, $-\omega$ is weak where $\partial s / \partial p$ is
486 positive at low levels in CAM while $-\omega$ is stronger where $\partial s / \partial p$ becomes negative aloft, yielding
487 positive Γ_V that contributes to s export. The SPCAM $-\omega$ profile is strikingly different than that in CAM
488 and, combined with a minimum of s at a higher pressure level, produces sharply negative Γ_V and s
489 import.

490 Further exploring intraseasonal fluctuations of NGMS, we present lagged linear regressions of
491 both anomalous and total NGMS in Figure 9. The index used is a time series of equatorial, MJO-
492 filtered, and standardized precipitation at 90°E . The plots represent the temporal behavior of the NGMS
493 components associated with a $+1\sigma$ change in the MJO rainfall index. In ERAI, both the horizontal and
494 vertical NGMS components are positively correlated with Γ_T , but Γ_V leads Γ_T by 3-7 days while Γ_H lags

495 Γ_T by ~ 1 -5 days (Fig. 9, top left). The negative Γ_T tendencies about 2-3 weeks prior to peak convection
496 are initially driven by Γ_V and are likely associated with the shallow cumulus and congestus regime that
497 imports s . Negative Γ_H lags the Γ_T minimum but sustains s import longer than if Γ_V were acting alone.
498 As peak convection develops near Day 0, Γ_V drives a rapid shift to positive Γ_T , the stratiform cloud
499 regime emerges, and export of s begins. The peak of Γ_H again lags Γ_T by a few days and is consistent
500 with strong low-level anomalous divergence linked to the westerly wind bursts, Rossby gyres, and
501 enhanced mixing due to synoptic disturbances (Benedict and Randall 2007, Maloney 2009). Import of
502 s —largely through negative Γ_V —redevelops two to three weeks after peak convection as the MJO
503 suppressed phase returns. Notably, anomalous fluctuations of Γ_V and Γ_H are of approximately the same
504 magnitude in ERAI. Observed NGMS fluctuations in the equatorial West Pacific (not shown) have
505 patterns similar to those in the east Indian Ocean but are of smaller magnitude.

506 Comparison of the GCM simulations to ERAI (Fig. 9, left column) reveals that the modified runs
507 produce qualitatively consistent results despite signals that may be less robust statistically, while the
508 control runs have weaker NGMS fluctuations and less realistic behavior. The modified simulations
509 generally foster larger fluctuations in NGMS anomalies, particularly those related to Γ_V , compared to the
510 control runs. In AM3-CTL and CAM, fluctuations of Γ_T are almost entirely driven by Γ_H while Γ_V plays
511 a much smaller role. Similar behavior is noted in both AM2-CTL and AM2-TOK (omitted), reaffirming
512 the poor east Indian Ocean MJO signal in those models (see Fig. 3). The interplay of NGMS
513 components is better captured in AM3-A, the version of AM3 that produces a more realistic MJO.

514 The right column of Fig. 9 shows the regressed form of the NGMS components with their
515 respective mean values included. Fluctuations associated with NGMS anomalies can represent large
516 percentages of the background NGMS. For example, the typical peak-to-trough difference of ~ 0.18 for
517 Γ_T in ERAI (Fig. 9, upper-left panel) is about 45% of the background value of ~ 0.40 estimated by

518 averaging Γ_T in the upper-right ERAI panel of Fig. 9 across all lag days. We obtain similar results for
519 ERAI Γ_H , but for Γ_V the fluctuations (~ 0.11) are larger than the background value itself ($\sim +0.05$).
520 Importantly, the fluctuating part of Γ_V is large enough to shift total Γ_V to values that are near zero or
521 slightly negative during the MJO suppressed phase, consistent with Haertel et al. (2008). The NGMS
522 fluctuations relative to the background NGMS in the GCM simulations varies widely. Anomaly
523 fluctuations of Γ_T and Γ_H constitute anywhere from 15% (AM3-CTL) to 150% (SPCAM) of the
524 background values. The fluctuating components represent larger percentages of the background NGMS
525 in the models that produce more realistic MJOs (in Fig. 9, AM3-A and SPCAM). In none of the
526 simulations are the magnitudes of NGMS fluctuations large enough to change the sign of the
527 background NGMS value over the MJO lifetime, perhaps suggesting that the background NGMS
528 magnitude and sign of the various NGMS components—rather than the intraseasonal anomalies of these
529 components—may be dominant in determining an MJO instability mechanism related to NGMS.

530 Following Neelin and Held (1987) and Maloney (2009), the budget of vertically integrated and
531 20-100-day bandpass-filtered s may be written:

$$T_R \left[\frac{\partial s}{\partial t} \right]_{\text{ISO}} = -T_R \left\{ \left[\omega \frac{\partial s}{\partial p} \right]_{\text{ISO}} + [\mathbf{v} \cdot \nabla s]_{\text{ISO}} \right\} + \text{LH}_{\text{ISO}} + \text{SH}_{\text{ISO}} + [\text{LW}]_{\text{ISO}} \quad (6)$$

532 In (6), subscript “ISO” signifies that variables have been 20-100-day bandpass filtered; LH and SH are
533 the surface latent and sensible heat fluxes, respectively; and LW is the longwave heating rate. Other
534 notation is the same as in previous equations. We omit negligible contributions to the s budget from
535 $[\text{SW}]_{\text{ISO}}$. Budget anomaly residuals are at most 7 W m^{-2} for ERAI, AM2-CTL, CAM, and SPCAM; 2
536 W m^{-2} for the AM3 runs; and 20 W m^{-2} for AM2-TOK. The first term in (6) represents the column-
537 integrated time tendency of s , and the second and third terms are the column-integrated export of s due
538 to vertical and horizontal advection, respectively. Figure 10 shows the s budget terms in (6) and the
539 precipitation anomaly composited based on all local maxima between the months of September and

540 April that exceed $+1\sigma$ in an ISO-filtered and standardized equatorial east Indian Ocean precipitation
541 index. Our findings are qualitatively similar for MJO events in the west Pacific Ocean (not shown). For
542 all data sets, the s time tendency term leads precipitation by 90° , where column s accumulates during
543 anomalously dry periods and is exhausted during heavy rainfall. In observations (Fig. 10a), the
544 advection terms are roughly 180° out of phase with LH, [LW], and precipitation. Consistent with the
545 results of Fig. 9, an increase of $[s]$ one to three weeks ahead of peak rainfall is associated with both
546 vertical and horizontal advection in observations (Fig. 10a). During heaviest rainfall, [LW] and LH
547 contribute strongly to positive time tendencies of $[s]$ while advection attempt to reduce $[s]$. These
548 temporal patterns of the s budget are reminiscent of the moist static energy budget composites reported
549 in Kiranmayi and Maloney (2011).

550 All simulated patterns of $[\partial s / \partial t]$ (Figs. 9b-g) are qualitatively consistent with observations
551 despite differences in the dominant terms on the rhs of (6). Both the AM2-CTL and AM3-CTL (Figs 9b
552 and 9d) produce budget patterns that are similar to observations, but in the corresponding modified
553 simulations (Figs. 9c and 9e) vertical advection contributes to positive time tendencies of $[s]$ during
554 heaviest rainfall, in contrast to both the controls runs and observations. The positive correlation between
555 vertical advection and precipitation is presumably what promotes a reduced GMS in the modified AM
556 run, and is also consistent with Figure 7. The unrealistic behavior in vertical advection working to
557 increase $[s]$ is offset by weaker LH and [LW] and an enhanced negative contribution from horizontal
558 advection, especially for AM2-TOK. Owing to the unrealistic advective tendencies in AM2-TOK (and
559 perhaps AM3-A), we question whether the stronger intraseasonal variability in that model is being
560 produced for reasons that are physically consistent with intraseasonal variability seen in ERAI. Small
561 horizontal and vertical advective tendencies result in unrealistically weak fluctuations in CAM (Fig. 9f).
562 The s budget terms are reproduced well in the SPCAM (Fig. 9g), with import of $[s]$ ahead of peak MJO

563 rainfall driven initially by vertical advection and subsequently horizontal advection as in observations
564 (Fig. 9a).

565

566 **Section 5. Conclusions and discussion**

567 This study reviews differences in normalized gross moist stability (NGMS) seen in a comparison
568 of three pairs of GCMs. In each GCM pair, one member produces weak intraseasonal variability while
569 the other produces stronger intraseasonal variability and more realistic MJO disturbances due to
570 modification in the treatment of deep convection. The assessment of NGMS and its horizontal and
571 vertical components is of interest because of the demonstrated link between NGMS and moisture modes,
572 convectively coupled disturbances that resemble the MJO and whose development and dynamics in
573 reduced-complexity models are closely linked to moisture perturbations (e.g., Sobel et al. 2001, Fuchs
574 and Raymond 2005, Sugiyama 2009). Moisture mode instability in these models occurs when NGMS—
575 or effective NGMS when accounting for additional contributions from other diabatic sources such as
576 surface fluxes and cloud-radiative feedbacks—is negative.

577 Previous studies have demonstrated a close connection between MJO-like disturbances, the
578 sensitivity of deep convection to tropospheric moisture, and GMS in conventional full-physics GCMs
579 (e.g., Frierson et al. 2011, Hannah and Maloney 2011). Recently, Pritchard and Bretherton (2013,
580 accepted pending major revisions) showed that more robust MJOs develop in the SP-CAM when
581 tropical vorticity anomalies and their contribution to horizontal moisture advection are artificially
582 amplified. Those authors, however, report ambiguous changes in GMS as a function of MJO
583 performance. Their results on GMS in this context are not as straightforward to interpret, since their
584 experiments with artificially increased horizontal advection modify the denominator of (4), making it
585 less direct of a measure of convective activity. Regardless, a more thorough understanding is needed of

586 the potential applicability of GMS as a diagnostic of the MJO. This study examines NGMS behavior
587 and its connection to tropical intraseasonal variability in a suite of full-physics GCMs that includes both
588 conventionally parameterized and superparameterized deep convection.

589 A consistent picture emerges between models with weak intraseasonal variability (“weak-ISV”)
590 and those with strong intraseasonal variability and more realistic MJOs (“strong-ISV”) in terms of their
591 time-mean total, horizontal, and vertical NGMS components (Γ_T , Γ_H , and Γ_V , respectively). Compared
592 to the control simulations, a reduction in winter-mean Γ_T in each modified simulation is driven by a
593 substantial reduction in Γ_V , while Γ_H remains similar to or slightly higher than its control simulation
594 value (Fig. 5). Values of Γ_T in the strong-ISV models are near zero or slightly positive across all Indo-
595 Pacific longitudes but are reduced from the values of their weak-ISV counterparts, while Γ_V shifts from
596 weakly positive to weakly or moderately negative between weak- and strong-ISV models. Raymond
597 and Fuchs (2009) compare a toy model with robust MJO activity and negative Γ_V to a model-derived
598 analysis product with weak intraseasonal variability and consistently positive Γ_V . They assert that the
599 improved MJO depiction in the toy model results from negative Γ_V tendencies that can induce moisture
600 mode instability. Less positive Γ_T values increase sensitivity of precipitation to entropy forcing in the
601 time mean [see (1)]. Additionally, smaller Γ_T , when combined with other diabatic sources of column
602 moist entropy, can result in effectively negative NGMS (Su and Neelin 2002; Bretherton and Sobel
603 2002; Sugiyama 2009) that would also foster moisture mode instability, the relevance of which has been
604 suggested by recent modeling studies and mechanism denial experiments (e.g. Maloney et al. 2010;
605 Landu and Maloney 2011, Andersen and Kuang 2012). Our results show a highly correlated linear
606 relationship between winter-mean and Warm Pool averaged Γ_V (or Γ_T) and the robustness of MJO
607 eastward propagation in the models (Fig. 6). In the simulations examined, east-to-west ratios of power
608 in the MJO spectral region increase as Γ_V decreases and becomes negative. No relationship exists

609 between Γ_H and the MJO metric, suggesting that the time-mean vertical NGMS component is more
610 closely tied to intraseasonal variability in the GCMs examined.

611 We also demonstrate connections between variations in NGMS and the MJO on subseasonal
612 time scales. In the reanalysis, export of vertically integrated moist entropy ($[s]$) by vertical advection
613 occurs when vertically integrated moisture convergence (VIMC) is positive and large, presumably in the
614 presence of mature cumulonimbi and their associated stratus clouds (Fig. 7, top). For shallower
615 convection when VIMC is only weakly positive, import of s occurs. Horizontal advection exports s
616 regardless of the sign and magnitude of VIMC. The relationship between VIMC and vertical and
617 horizontal exports of s differs among the GCM simulations examined (Fig. 7, lower panels). We
618 provide plausible reasons for why this inconsistency arises (Sec. 4), but further investigation will be left
619 for future studies.

620 We show that the efficiency with which s is imported into the column during the suppressed
621 MJO phase is model-dependent and is effectively portrayed by viewing profiles of s and vertical
622 pressure velocity $-\omega$ (Fig. 8). In AM2 (omitted) and AM3 (Fig. 8, top), the reduction in Γ_V and thus the
623 stronger import of s in the modified simulations results from a stronger bottom-heavy $-\omega$ profile, while
624 the s profiles show similar patterns. For the CAM/SPCAM comparison, however, the shift of the s
625 minimum to lower heights—despite a more realistic $-\omega$ profile—results in a less negative Γ_V and weaker
626 s import in CAM.

627 NGMS is not fixed in time but instead can change substantially on intraseasonal time scales.
628 During the MJO suppressed phase, negative anomalies of Γ_T are driven initially by Γ_V and sustained by
629 Γ_H (Fig. 9). During the MJO active phase, Γ_V drives positive anomalies of Γ_T that are again sustained by
630 Γ_H . Fluctuations of anomalous NGMS components associated with the MJO can be 0.1-0.2 in
631 magnitude and can represent large fractions of the background NGMS magnitude, particularly for Γ_V .

632 Anomalous NGMS indeed modulates the magnitude of background NGMS, but in only one instance
633 (ERA-Interim Γ_{ν}) the fluctuations were large enough to change the sign of the total form of that NGMS
634 component. As mentioned earlier, additional diabatic sources may create an effectively negative NGMS
635 even if background NGMS remains weakly positive (Su and Neelin 2002, Sobel and Bretherton 2002,
636 Sugiyama 2009). A more rigorous analysis of the contributions to effective NGMS by these diabatic
637 sources is deferred to future GCM studies.

638 Analysis of the s budget in the composite MJO underscores the critical role that advection plays
639 in the accumulation of s ahead of peak MJO rainfall (Fig. 10). Fluxes of surface latent heating and
640 vertically integrated longwave radiation are in phase with precipitation, suggesting that the advective
641 tendencies are the primary drivers of changes in $[s]$ and precipitation. Consistent with the behavior of
642 regressed NGMS components relative to the MJO (Fig. 9), vertical and then horizontal advection drive a
643 positive time tendency of $[s]$ which itself leads positive precipitation anomalies. Unrealistic profiles of
644 vertical advection are seen in AM2-TOK and to a lesser extent in AM3-A, but all budget terms in
645 SPCAM closely match those in ERA-Interim.

646 We have demonstrated that the development of more robust MJO disturbances in GCMs with
647 modified deep convection schemes is associated with reductions in total NGMS driven primarily by the
648 vertical NGMS advective component rather than the horizontal component. Anomalous NGMS
649 fluctuations associated with the MJO can strongly modulate the magnitude of the background NGMS as
650 well, although shifts from positive to negative values are only seen in the vertical NGMS component in
651 the reanalysis data set and not in any of the simulations examined. The sign of NGMS is primarily a
652 function of the time mean while its magnitude changes substantially during the passage of MJO
653 disturbances. Exactly how the NGMS magnitude fluctuations affect moisture mode instability and the
654 MJO initiation and maintenance remains a topic of great interest. Additional research that examines the

655 detailed role that surface moist entropy fluxes, cloud-radiative feedbacks, and other diabatic sources
656 play in influencing vertically integrated moist entropy will also provide greater insight into the impact of
657 effectively negative NGMS on the MJO.

658

659 *Acknowledgements.* We would like to thank David Raymond and the WGNE MJO Task Force for their
660 scientific advice and motivation of this work. This work was supported by awards NA08OAR4320893,
661 NA12OAR4310077 (JJB, EDM) and NA08OAR4320912 (AHS) from the National Oceanic and
662 Atmospheric Administration, U.S. Department of Commerce, and by the Climate and Large-Scale
663 Dynamics Program of the National Science Foundation under Grants AGS-1025584, AGS-1062161, and
664 AGS-0946911 (EDM). The statements, findings, conclusions, and recommendations do not necessarily
665 reflect the views of NSF, NOAA, or the Department of Commerce.

666 **References**

- 667 Adler, R. F., and Coauthors, 2003: The version-2 global precipitation climatology project (GPCP)
668 monthly precipitation analysis (1979-present). *J. Hydrol.*, **4**, 1147-1167.
- 669 Andersen, J. A., and Z. M. Kuang, 2012: Moist Static Energy Budget of MJO-like Disturbances in the
670 Atmosphere of a Zonally Symmetric Aquaplanet. *J. Climate*, **25**, 2782-2804.
- 671 Anderson, J. L., and Coauthors, 2004: The new GFDL global atmosphere and land model AM2-LM2:
672 Evaluation with prescribed SST simulations. *J. Climate*, **17**, 4641-4673.
- 673 Arakawa, A., 2004: The Cumulus Parameterization Problem: Past, Present, and Future. *J. Climate*, **17**,
674 2493-2525.
- 675 Back, L. E., and C. S. Bretherton, 2006: Geographic variability in the export of moist static energy and
676 vertical motion profiles in the tropical Pacific. *Geophys Res Lett*, **33**.
- 677 Benedict, J. J., E. D. Maloney, A. H. Sobel, D. M. Frierson, and L. J. Donner, 2013: Tropical
678 Intraseasonal Variability in Version 3 of the GFDL Atmosphere Model. *J. Climate*, **26**, 426-449.
- 679 Benedict, J. J., and D. A. Randall, 2007: Observed Characteristics of the MJO Relative to Maximum
680 Rainfall. *J. Atmos. Sci.*, **64**, 2332-2354.
- 681 Benedict, J. J., and D. A. Randall, 2009: Structure of the Madden-Julian Oscillation in the
682 Superparameterized CAM. *J. Atmos. Sci.*, **66**, 3277-3296.
- 683 Berrisford, P., and Coauthors, 2009: The ERA-Interim Archive, ECMWF Tech. Rep. 1, 16 pp. [Online
684 at http://www.ecmwf.int/publications/library/ecpublications/_pdf/era/era_report_series/RS_1.pdf.]
- 685 Bony, S., and K. A. Emanuel, 2005: On the Role of Moist Processes in Tropical Intraseasonal
686 Variability: Cloud-Radiation and Moisture-Convection Feedbacks. *J. Atmos. Sci.*, **62**, 2770-2789.
- 687 Bretherton, C. S., P. N. Blossey, and M. Khairoutdinov, 2005: An energy-balance analysis of deep
688 convective self-aggregation above uniform SST. *J. Atmos. Sci.*, **62**, 4273-4292.

689 Bretherton, C. S., M. E. Peters, and L. E. Back, 2004: Relationships between water vapor path and
690 precipitation over the tropical oceans. *J. Climate*, **17**, 1517-1528.

691 Bretherton, C. S., and A. H. Sobel, 2002: A simple model of a convectively coupled walker circulation
692 using the weak temperature gradient approximation. *J. Climate*, **15**, 2907-2920.

693 Carrillo, C. L., and D. J. Raymond, 2005: Moisture tendency equations in a tropical atmosphere. *J.*
694 *Atmos. Sci.*, **62**, 1601-1613.

695 Charney, J. G., 1963: A Note on Large-Scale Motions in the Tropics. *J. Atmos. Sci.*, **20**, 607-609.

696 CLIVAR_MJO_Working_Group, 2009: MJO Simulation Diagnostics. *J. Climate*, **22**, 3006-3030.

697 Collins, W. D., and Coauthors, 2006: The Formulation and Atmospheric Simulation of the Community
698 Atmosphere Model Version 3 (CAM3). *J. Climate*, **19**, 2144-2161.

699 Derbyshire, S. H., I. Beau, P. Bechtold, J. Y. Grandpeix, J. M. Piriou, J. L. Redelsperger, and P. M. M.
700 Soares, 2004: Sensitivity of moist convection to environmental humidity. *Quart. J. Roy. Meteor.*
701 *Soc.*, **130**, 3055-3079.

702 Donner, L. J., C. J. Seman, R. S. Hemler, and S. M. Fan, 2001: A cumulus parameterization including
703 mass fluxes, convective vertical velocities, and mesoscale effects: Thermodynamic and
704 hydrological aspects in a general circulation model. *J. Climate*, **14**, 3444-3463.

705 Donner, L. J., and Coauthors, 2011: The Dynamical Core, Physical Parameterizations, and Basic
706 Simulation Characteristics of the Atmospheric Component AM3 of the GFDL Global Coupled
707 Model CM3. *J. Climate*, **24**, 3484-3519.

708 Emanuel, K. A., J. D. Neelin, and C. S. Bretherton, 1994: On Large-Scale Circulations in Convecting
709 Atmospheres. *Quart. J. Roy. Meteor. Soc.*, **120**, 1111-1143.

710 Frierson, D. M. W., 2007: Convectively Coupled Kelvin Waves in an Idealized Moist General
711 Circulation Model. *J. Atmos. Sci.*, **64**, 2076-2090.

712 Frierson, D. M. W., D. Kim, I. S. Kang, M. I. Lee, and J. L. Lin, 2011: Structure of AGCM-Simulated
713 Convectively Coupled Kelvin Waves and Sensitivity to Convective Parameterization. *J. Atmos.*
714 *Sci.*, **68**, 26-45.

715 Fuchs, Z., and D. J. Raymond, 2002: Large-scale modes of a nonrotating atmosphere with water vapor
716 and cloud-radiation feedbacks. *J. Atmos. Sci.*, **59**, 1669-1679.

717 ———, 2005: Large-scale modes in a rotating atmosphere with radiative-convective instability and
718 WISHE. *J. Atmos. Sci.*, **62**, 4084-4094.

719 Grabowski, W. W., and M. W. Moncrieff, 2004: Moisture-convection feedback in the tropics. *Quart. J.*
720 *Roy. Meteor. Soc.*, **130**, 3081-3104.

721 Haertel, P. T., G. N. Kiladis, A. Denno, and T. M. Rickenbach, 2008: Vertical-mode decompositions of
722 2-day waves and the Madden-Julian oscillation. *J. Atmos. Sci.*, **65**, 813-833.

723 Hagos, S., L. R. Leung, and J. Dudhia, 2011: Thermodynamics of the Madden-Julian Oscillation in a
724 Regional Model with Constrained Moisture. *J. Atmos. Sci.*, **68**, 1974-1989.

725 Hannah, W. M., and E. D. Maloney, 2011: The Role of Moisture-Convection Feedbacks in Simulating
726 the Madden-Julian Oscillation. *J. Climate*, **24**, 2754-2770.

727 Held, I. M., and B. J. Hoskins, 1985: Large-Scale Eddies and the General-Circulation of the
728 Troposphere. *Adv Geophys*, **28**, 3-31.

729 Holloway, C. E., and J. D. Neelin, 2009: Moisture Vertical Structure, Column Water Vapor, and
730 Tropical Deep Convection. *J. Atmos. Sci.*, **66**, 1665-1683.

731 Huffman, G. J., and Coauthors, 2007: The TRMM Multisatellite Precipitation Analysis (TMPA): Quasi-
732 Global, Multiyear, Combined-Sensor Precipitation Estimates at Fine Scales. *J. Hydrol.*, **8**, 38-55.

733 Hurrell, J. W., J. J. Hack, D. Shea, J. M. Caron, and J. Rosinski, 2008: A New Sea Surface Temperature
734 and Sea Ice Boundary Dataset for the Community Atmosphere Model. *J. Climate*, **21**, 5145-5153.

735 Inness, P. M., J. M. Slingo, E. Guilyardi, and J. Cole, 2003: Simulation of the Madden-Julian oscillation
736 in a coupled general circulation model. Part II: The role of the basic state. *J. Climate*, **16**, 365-382.

737 Khairoutdinov, M., C. DeMott, and D. Randall, 2008: Evaluation of the Simulated Interannual and
738 Subseasonal Variability in an AMIP-Style Simulation Using the CSU Multiscale Modeling
739 Framework. *J. Climate*, **21**, 413-431.

740 Khairoutdinov, M., D. Randall, and C. DeMott, 2005: Simulations of the Atmospheric General
741 Circulation Using a Cloud-Resolving Model as a Superparameterization of Physical Processes. *J.*
742 *Atmos. Sci.*, **62**, 2136-2154.

743 Khouider, B., and A. J. Majda, 2006: A simple multcloud parameterization for convectively coupled
744 tropical waves. Part I: Linear analysis. *J. Atmos. Sci.*, **63**, 1308-1323.

745 Kim, D., A. H. Sobel, E. D. Maloney, D. M. W. Frierson, and I.-S. Kang, 2011: A Systematic
746 Relationship between Intraseasonal Variability and Mean State Bias in AGCM Simulations. *J.*
747 *Climate*, **24**, 5506-5520.

748 Kim, D., M.-I. Lee, D. Kim, S. Schubert, D. E. Waliser, and B. Tian, 2013a: Representation of tropical
749 subseasonal variability of precipitation in global reanalyses. Submitted to *Climate Dyn.*

750 Kim, D., and Coauthors, 2013b: Process-oriented MJO Simulation Diagnostic: Moisture Sensitivity of
751 Simulated Convection. Submitted to *J. Climate*.

752 Kim, D., and Coauthors, 2009: Application of MJO Simulation Diagnostics to Climate Models. *J.*
753 *Climate*, **22**, 6413-6436.

754 Kiranmayi, L., and E. D. Maloney, 2011: Intraseasonal moist static energy budget in reanalysis data. *J.*
755 *Geophys Res-Atmos*, **116**.

756 Kuang, Z. M., 2008: A moisture-stratiform instability for convectively coupled waves. *J. Atmos. Sci.*,
757 **65**, 834-854.

758 ———, 2011: The Wavelength Dependence of the Gross Moist Stability and the Scale Selection in the
759 Instability of Column-Integrated Moist Static Energy. *J. Atmos. Sci.*, **68**, 61-74.

760 ———, 2012: Weakly Forced Mock Walker Cells. *J. Atmos. Sci.*, **69**, 2759-2786.

761 Landu, K., and E. D. Maloney, 2011: Effect of SST Distribution and Radiative Feedbacks on the
762 Simulation of Intraseasonal Variability in an Aquaplanet GCM. *J. Meteor. Soc. Japan*, **89**, 195-
763 210.

764 Lucas, C., E. J. Zipser, and B. S. Ferrier, 2000: Sensitivity of tropical west pacific oceanic squall lines to
765 tropospheric wind and moisture profiles. *J. Atmos. Sci.*, **57**, 2351-2373.

766 Madden, R. A., and P. R. Julian, 1971: Detection of a 40-50 Day Oscillation in the Zonal Wind in the
767 Tropical Pacific. *J. Atmos. Sci.*, **28**, 702-708.

768 Majda, A. J., and B. Khouider, 2004: A model for convectively coupled tropical waves: Nonlinearity,
769 rotation, and comparison with observations. *J. Atmos. Sci.*, **61**, 2188-2205.

770 Maloney, E. D., 2009: The Moist Static Energy Budget of a Composite Tropical Intraseasonal
771 Oscillation in a Climate Model. *J. Climate*, **22**, 711-729.

772 Maloney, E. D., A. H. Sobel, and W. M. Hannah, 2010: Intraseasonal Variability in an Aquaplanet
773 General Circulation. *J. Adv. Model. Earth Syst.*, **2**, Article #5, 24 pp.

774 Mapes, B. E., 2000: Convective Inhibition, Subgrid-Scale Triggering Energy, and Stratiform Instability
775 in a Toy Tropical Wave Model. *J. Atmos. Sci.*, **57**, 1515-1535.

776 Mapes, B. E., and J. T. Bacmeister, 2012: Diagnosis of Tropical Biases and the MJO from Patterns in
777 the MERRA Analysis Tendency Fields. *J. Climate*, **25**, 6202-6214.

778 Moorthi, S., and M. J. Suarez, 1992: Relaxed Arakawa-Schubert - a Parameterization of Moist
779 Convection for General-Circulation Models. *Mon. Wea. Rev.*, **120**, 978-1002.

780 Neelin, J. D., and I. M. Held, 1987: Modeling Tropical Convergence Based on the Moist Static Energy
781 Budget. *Mon. Wea. Rev.*, **115**, 3-12.

782 Neelin, J. D., and J. Y. Yu, 1994: Modes of Tropical Variability under Convective Adjustment and the
783 Madden-Julian Oscillation .1. Analytical Theory. *J. Atmos. Sci.*, **51**, 1876-1894.

784 Neelin, J. D., and N. Zeng, 2000: A quasi-equilibrium tropical circulation model - Formulation. *J.*
785 *Atmos. Sci.*, **57**, 1741-1766.

786 Peters, M. E., Z. M. Kuang, and C. C. Walker, 2008: Analysis of Atmospheric Energy Transport in
787 ERA-40 and Implications for Simple Models of the Mean Tropical Circulation. *J. Climate*, **21**,
788 5229-5241.

789 Raymond, D. J., 2000: Thermodynamic control of tropical rainfall. *Quart. J. Roy. Meteor. Soc.*, **126**,
790 889-898.

791 Raymond, D. J., and Z. Fuchs, 2007: Convectively coupled gravity and moisture modes in a simple
792 atmospheric model. *Tellus A*, **59**, 627-640.

793 ———, 2009: Moisture Modes and the Madden-Julian Oscillation. *J. Climate*, **22**, 3031-3046.

794 ———, 2013: Moist Entropy in Atmospheric Modeling. Submitted to *J. Adv. Model. Earth Syst.*

795 Raymond, D. J., S. Sessions, A. Sobel, and Z. Fuchs, 2009: The Mechanics of Gross Moist Stability. *J.*
796 *Adv. Model. Earth Syst.*, **1**, Article #9, 20 pp.

797 Raymond, D. J., and S. L. Sessions, 2007: Evolution of convection during tropical cyclogenesis.
798 *Geophys. Res. Lett.*, **34**.

799 Raymond, D. J., S. L. Sessions, and Z. Fuchs, 2007: A theory for the spinup of tropical depressions.
800 *Quart. J. Roy. Meteor. Soc.*, **133**, 1743-1754.

801 Raymond, D. J., and X. P. Zeng, 2005: Modelling tropical atmospheric convection in the context of the
802 weak temperature gradient approximation. *Quart. J. Roy. Meteor. Soc.*, **131**, 1301-1320.

803 Reynolds, R. W., N. A. Rayner, T. M. Smith, D. C. Stokes, and W. Wang, 2002: An Improved In Situ
804 and Satellite SST Analysis for Climate. *J. Climate*, **15**, 1609-1625.

805 Salby, M. L., and H. H. Hendon, 1994: Intraseasonal Behavior of Clouds, Temperature, and Motion in
806 the Tropics. *J. Atmos. Sci.*, **51**, 2207-2224.

807 Sessions, S. L., S. Sugaya, D. J. Raymond, and A. H. Sobel, 2010: Multiple equilibria in a cloud-
808 resolving model using the weak temperature gradient approximation. *J. Geophys. Res.-Atmos.*,
809 **115**.

810 Sherwood, S. C., 1999: Convective precursors and predictability in the tropical western Pacific. *Mon.*
811 *Wea. Rev.*, **127**, 2977-2991.

812 Sobel, A., and E. Maloney, 2012: An Idealized Semi-Empirical Framework for Modeling the Madden-
813 Julian Oscillation. *J. Atmos. Sci.*, **69**, 1691-1705.

814 ———, 2013: Moisture Modes and the Eastward Propagation of the MJO. *J. Atmos. Sci.*, **70**, 187-192.

815 Sobel, A. H., G. Bellon, and J. Bacmeister, 2007: Multiple equilibria in a single-column model of the
816 tropical atmosphere. *Geophys. Res. Lett.*, **34**.

817 Sobel, A. H., E. D. Maloney, G. Bellon, and D. M. Frierson, 2010: Surface fluxes and tropical
818 intraseasonal variability: a reassessment. *J. Adv. Model. Earth Syst.*, **2**, Article #2, 27 pp.

819 Sobel, A. H., J. Nilsson, and L. M. Polvani, 2001: The weak temperature gradient approximation and
820 balanced tropical moisture waves. *J. Atmos. Sci.*, **58**, 3650-3665.

821 Su, H., and J. D. Neelin, 2002: Teleconnection mechanisms for tropical Pacific descent anomalies
822 during El Nino. *J. Atmos. Sci.*, **59**, 2694-2712.

823 Sugiyama, M., 2009: The Moisture Mode in the Quasi-Equilibrium Tropical Circulation Model. Part I:
824 Analysis Based on the Weak Temperature Gradient Approximation. *J. Atmos. Sci.*, **66**, 1507-1523.

825 Thayer-Calder, K., and D. A. Randall, 2009: The Role of Convective Moistening in the Madden-Julian
826 Oscillation. *J. Atmos. Sci.*, **66**, 3297-3312.

827 Tokioka, T., K. Yamazaki, A. Kitoh, and T. Ose, 1988: The Equatorial 30-60 Day Oscillation and the
828 Arakawa-Schubert Penetrative Cumulus Parameterization. *J. Meteor. Soc. Japan*, **66**, 883-901.

829 Wang, S., and A. H. Sobel, 2011: Response of convection to relative sea surface temperature: Cloud-
830 resolving simulations in two and three dimensions. *J. Geophys. Res.-Atmos.*, **116**. D11119,
831 doi:10.1029/2010JD015347.

832 ———, 2012: Impact of imposed drying on deep convection in a cloud-resolving model. *J. Geophys. Res.-*
833 *Atmos.*, **117**. D11119, doi:10.1029/2010JD015347.

834 Wheeler, M., and G. N. Kiladis, 1999: Convectively Coupled Equatorial Waves: Analysis of Clouds and
835 Temperature in the Wavenumber-Frequency Domain. *J. Atmos. Sci.*, **56**, 374-399.

836 Yu, L. S., and R. A. Weller, 2007: Objectively analyzed air-sea heat fluxes for the global ice-free oceans
837 (1981-2005). *Bull. Amer. Meteor. Soc.*, **88**, 527-539.

838 Zhang, C., 2005: Madden-Julian Oscillation. *Rev. Geophys.*, **43**, 2004RG000158.

839 Zhang, C., and Coauthors, 2006: Simulations of the Madden-Julian oscillation in four pairs of coupled
840 and uncoupled global models. *Climate Dyn.*, **27**, 573-592.

841 Zhang, G. J., 2002: Convective quasi-equilibrium in midlatitude continental environment and its effect
842 on convective parameterization. *J. Geophys. Res.*, **107**, 4220.

843 Zhang, G. J., and N. A. Mcfarlane, 1995: Sensitivity of Climate Simulations to the Parameterization of
844 Cumulus Convection in the Canadian Climate Center General-Circulation Model. *Atmos. Ocean*,
845 **33**, 407-446.

846

847 **Figure Captions**

848

849 **Figure 1.** (a) October-April mean GPCP precipitation (shading) and ERAI U_{850} (contours). Wind
850 contours are 0, ± 2 , ± 4 , ± 8 , and ± 12 m s^{-1} and positive (zero, negative) contours are thin solid (thick
851 solid, dashed) lines. (b-g) October-April mean precipitation differences between each model and GPCP
852 (shaded), and October-April mean U_{850} using identical contours as in (a).

853

854 **Figure 2.** Frequency-zonal wavenumber power spectra of the component (about the equator) of
855 precipitation for (a) TRMM and (b-g) the GCM simulations. Displayed is the base-10 logarithm of the
856 summation of power between 15°S and 15°N .

857

858 **Figure 3.** Lag correlations of U_{850} with precipitation at (left) 90°E and (right) 150°E . Fields are 20-
859 100-day filtered and averaged between 15°S and 15°N . Solid (dashed) contours represent positive
860 (negative) correlations that are shaded dark (light) gray if they exceed the 95% statistical significance
861 level. Observed wind and rainfall fields are taken from ERAI and TRMM, respectively. In the left
862 panels, index reference longitudes and the 5 m s^{-1} phase speed are marked by vertical and slanted thick
863 lines, respectively. Right panels also contain the 10 m s^{-1} phase speed line.

864

865 **Figure 4.** ERAI October-April mean (a) horizontal $T_R[\mathbf{v} \cdot \nabla s]$, (b) vertical $T_R[\omega \partial s / \partial p]$, and (c) total
866 $T_R[\mathbf{v} \cdot \nabla s + \omega \partial s / \partial p]$ column-integrated moist entropy export, shown in color shading. In all panels,
867 thin (thick) contours represent the 3 (6) mm d^{-1} mean precipitation.

868

869 **Figure 5.** October-April means of selected advective and diabatic terms related to GMS in the (l-r)
870 AM2, AM3, and CAM/SPCAM. Variables have been latitudinally averaged over a chosen Indo-Pacific

871 domain where climatological vertically integrated moisture convergence is positive (see text). In each
872 panel, solid black (dashed black, gray) lines represent observations (control simulation, modified
873 simulation). Variables shown are (top-bottom) horizontal, vertical, and total GMS advection terms (in
874 W m^{-2}); their counterparts normalized by column moisture convergence (unitless); column moisture
875 convergence (in W m^{-2}); and precipitation (in mm d^{-1}).

876

877 **Figure 6.** The relationship between October-April mean Γ_V and one metric of the robustness of MJO
878 eastward propagation. Spatial averaging to include only oceanic points within the climatological
879 convective region (see text) has been applied to Γ_V . The MJO metric is the ratio of eastward to
880 westward tropical rainfall power within the MJO spectral region [periods 30-96 days, zonal
881 wavenumbers +1 to +3 (eastward) or -1 to -3 (westward)]. Also shown are the best-fit line equation
882 and correlation coefficient r .

883

884 **Figure 7.** Horizontal (dark bullets) and vertical (light stars) advective components of vertically
885 integrated moist entropy divergence versus VIMC averaged over the east Indian Ocean region (70°-
886 100°E, 10°S-5°N) during October-April. Conditional sampling has been done to include only times
887 when the 91-day windowed variance of a precipitation index (i.e., rainfall averaged over the east Indian
888 Ocean region and then 20-100-day filtered) is greater than its winter average value. Land points are
889 omitted from the spatial averages. Each point represents a single day. Thick black best-fit lines are
890 overlaid, and the corresponding equations and correlation coefficients r appear at the bottom of each
891 panel. Starred r values are statistically significant above the 95% confidence level.

892

893 **Figure 8.** MJO suppressed-phase profiles of (left) moist entropy s and (right) pressure velocity $-\omega$
894 normalized by the value of peak upward motion for (top) AM3 and (bottom) CAM/SPCAM simulations.
895 Profiles are conditionally averaged over the equatorial east Indian Ocean (85° - 95°) to include only those
896 days between October and April in which a MJO rainfall index is less than -1σ . We use 20-100-day
897 filtered and standardized east Indian Ocean rainfall as our index.

898

899 **Figure 9.** (left) Anomalous and (right) total NGMS linearly regressed onto an MJO precipitation index
900 at 90° E. Regression time series index is defined as 20-100-day filtered (“MJO-filtered”) and
901 standardized precipitation averaged between 10° S- 10° N at 90° E. Each plot shows the total (NGMS-T,
902 or Γ_T ; black), vertical (NGMS-V, or Γ_V ; dark gray), and horizontal (NGMS-H, or Γ_H ; light gray)
903 components of NGMS. Regressed variables have been averaged to include only those latitudes where
904 climatological VIMC is positive (see text). For anomaly plots, variables are MJO-filtered departures
905 from the calendar-day mean. Dotted line sections denote values that are statistically significant above
906 the 92.5% level. Lag days appear along x-axis, and negative lag days occur before maxima in the MJO
907 rainfall index.

908

909 **Figure 10.** Budget of equatorial (15° S- 10° N) moist entropy based on a composite of winter (Sep-Apr)
910 MJO events in the east Indian Ocean for (a) ERAI/TRMM and (b-g) GCM simulations. All variables
911 are 20-100-day filtered and are shown in energy units (W m^{-2}). MJO events are defined as local
912 maxima that exceed $+1\sigma$ in a MJO-filtered and standardized east Indian Ocean precipitation index. Left
913 y-axis scale is for terms contributing to the moist entropy budget and the right y-axis scale is for
914 precipitation P (solid blue line in each panel). Lag days are at the bottom of each panel, with negative
915 days occurring before the MJO peak rainfall. Composite sample sizes appear at the upper right of each

916 panel. Square brackets represent vertical integrals from the surface to 100 hPa. Vertically integrated
917 shortwave heating is negligible and is omitted.

918

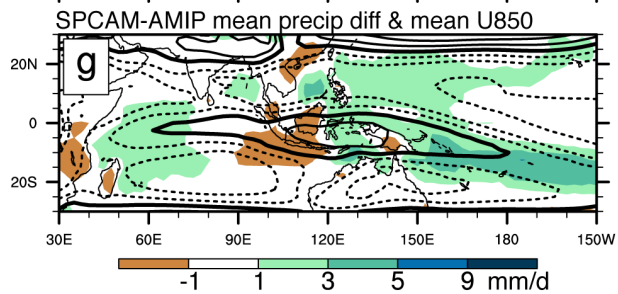
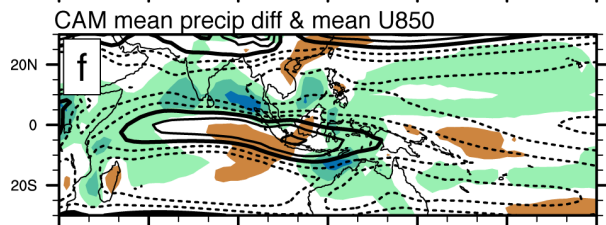
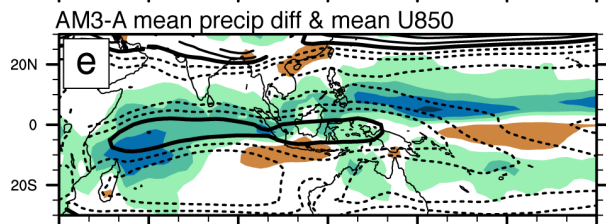
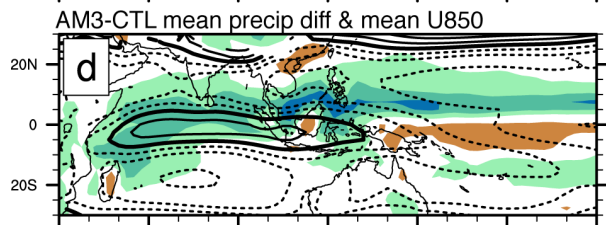
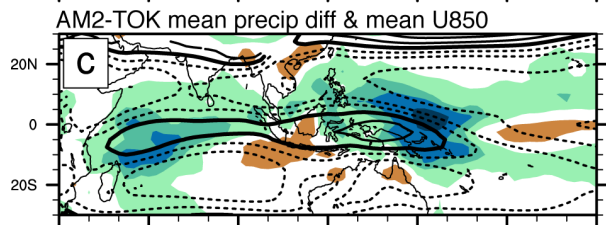
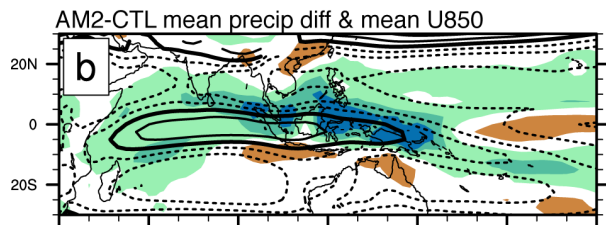
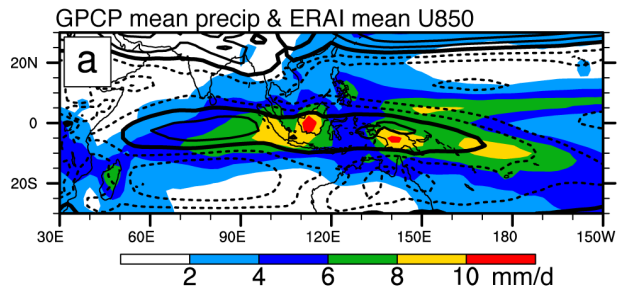
919 Table 1. Highlighted features of the GCMs examined in this study. Here, “L” represents the number of
 920 GCM levels, “RAS” is the Relaxed Arakawa-Schubert scheme of Moorthi and Suarez (1992), “ZM95”
 921 is the Zhang-McFarlane (1995) scheme, α is the Tokioka (1988) parameter, and “ISV” qualitatively
 922 describes intraseasonal variability within the simulation. See text for further details.

923

Model	GCM Resolution	Deep Convection Parameterization				ISV
		Scheme	Closure	Trigger	Downdrafts?	
AM2-CTL	2° lat × 2.5° lon, L24	RAS	CAPE relaxation	$\alpha = 0.025$	No	Weak
AM2-TOK	2° lat × 2.5° lon, L24	RAS	CAPE relaxation	$\alpha = 0.1$	No	Strong
AM3-CTL	~163-231 km, L32	Donner	CAPE relaxation	—	No	Weak
AM3-A	~163-231 km, L32	Donner	Zhang (2002) (CAPE-based)	Time-integrated low-level parcel lifting	Yes	Strong
CAM3.0	T42 (~2.8° × 2.8°), L30	ZM95	CAPE consumed at specified rate	—	Yes	Weak
SPCAM- AMIP	T42 (~2.8° × 2.8°), L30	Explicit (4-km CRM)	—	—	Explicit	Strong

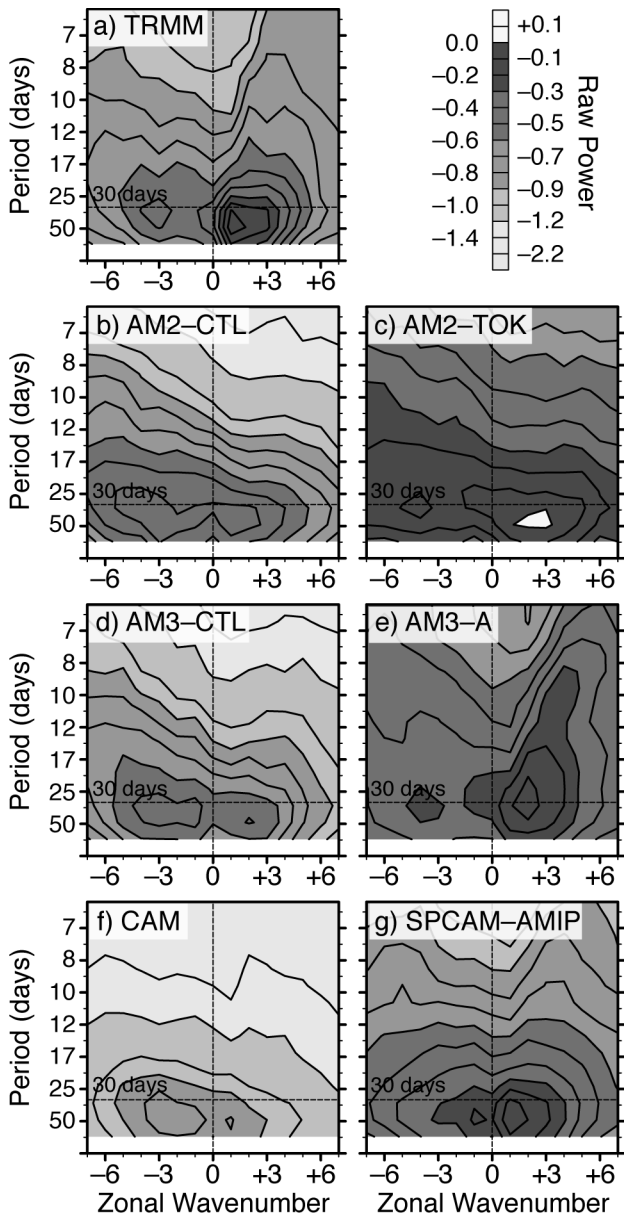
924

925



927

928 **Figure 1.** (a) October-April mean GPCP precipitation (shading) and ERAI U_{850} (contours). Wind
929 contours are 0, ± 2 , ± 4 , ± 8 , and ± 12 m s^{-1} and positive (zero, negative) contours are thin solid (thick
930 solid, dashed) lines. (b-g) October-April mean precipitation differences between each model and GPCP
931 (shaded), and October-April mean U_{850} using identical contours as in (a).

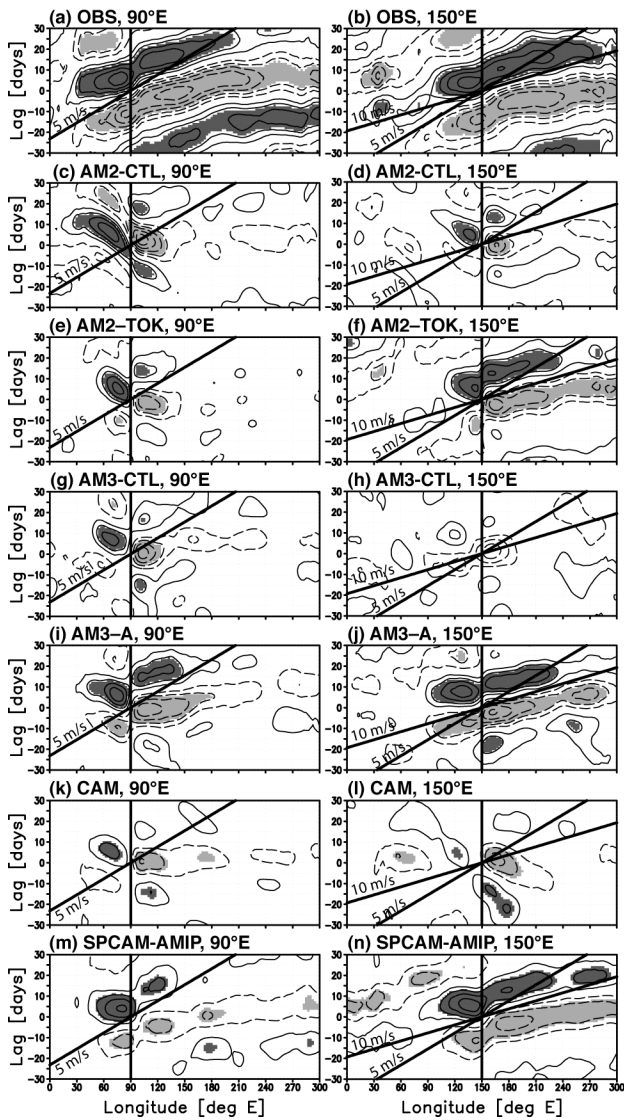


932

933 **Figure 2.** Frequency-zonal wavenumber power spectra of the component (about the equator) of
 934 precipitation for (a) TRMM and (b-g) the GCM simulations. Displayed is the base-10 logarithm of the
 935 summation of power between 15°S and 15°N.

936

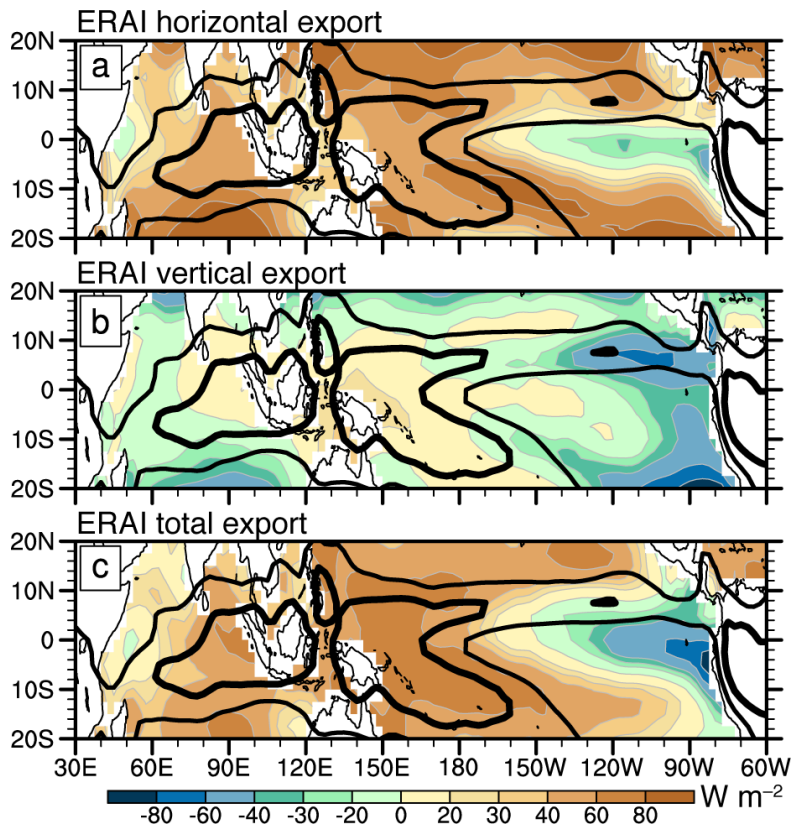
Lag correlation, U850 with Precipitation



937

938

939 **Figure 3.** Lag correlations of U_{850} with precipitation at (left) 90°E and (right) 150°E . Fields are 20-
 940 100-day filtered and averaged between 15°S and 15°N . Solid (dashed) contours represent positive
 941 (negative) correlations that are shaded dark (light) gray if they exceed the 95% statistical significance
 942 level. Observed wind and rainfall fields are taken from ERAI and TRMM, respectively. In the left
 943 panels, index reference longitudes and the 5 m s^{-1} phase speed are marked by vertical and slanted thick
 944 lines, respectively. Right panels also contain the 10 m s^{-1} phase speed line.

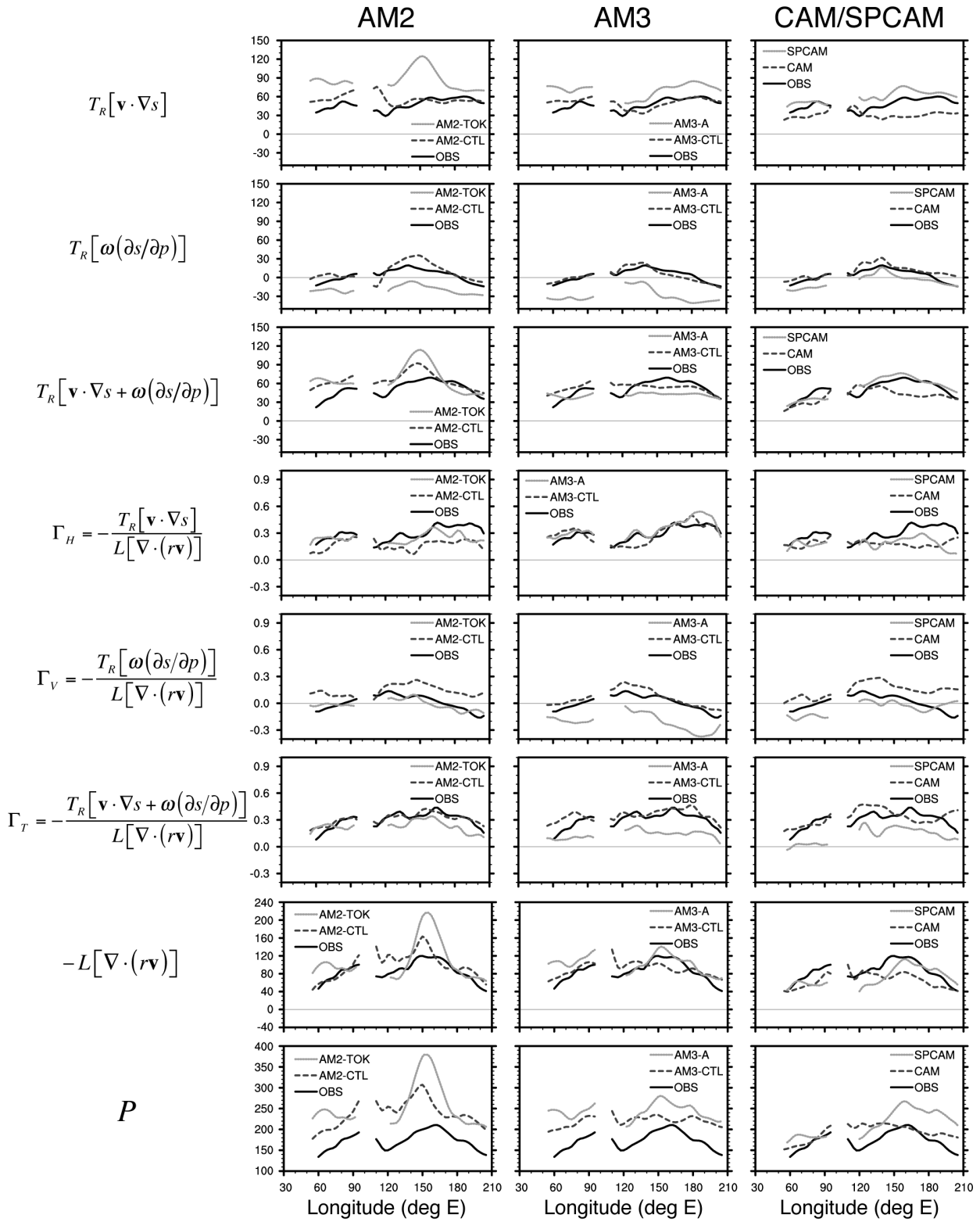


945

946

947 **Figure 4.** ERAI October-April mean (a) horizontal $T_R[\mathbf{v} \cdot \nabla s]$, (b) vertical $T_R[\omega \partial s / \partial p]$, and (c) total
 948 $T_R[\mathbf{v} \cdot \nabla s + \omega \partial s / \partial p]$ column-integrated moist entropy export, shown in color shading. In all panels,
 949 thin (thick) contours represent the 3 (6) mm d^{-1} mean precipitation.

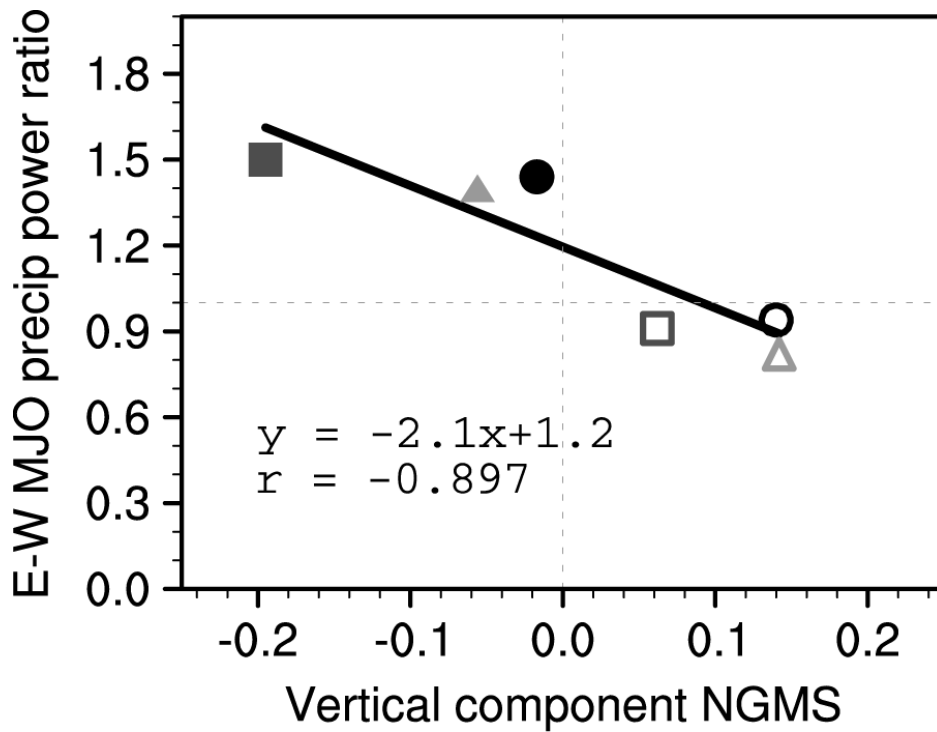
950



951

952

953 **Figure 5.** October-April means of selected advective and diabatic terms related to GMS in the (l-r)
954 AM2, AM3, and CAM/SPCAM. Variables have been latitudinally averaged over a chosen Indo-Pacific
955 domain where climatological vertically integrated moisture convergence is positive (see text). In each
956 panel, solid black (dashed black, gray) lines represent observations (control simulation, modified
957 simulation). Variables shown are (top-bottom) horizontal, vertical, and total GMS advection terms (in
958 W m^{-2}); their counterparts normalized by column moisture convergence (unitless); column moisture
959 convergence (in W m^{-2}); and precipitation (in mm d^{-1}).
960



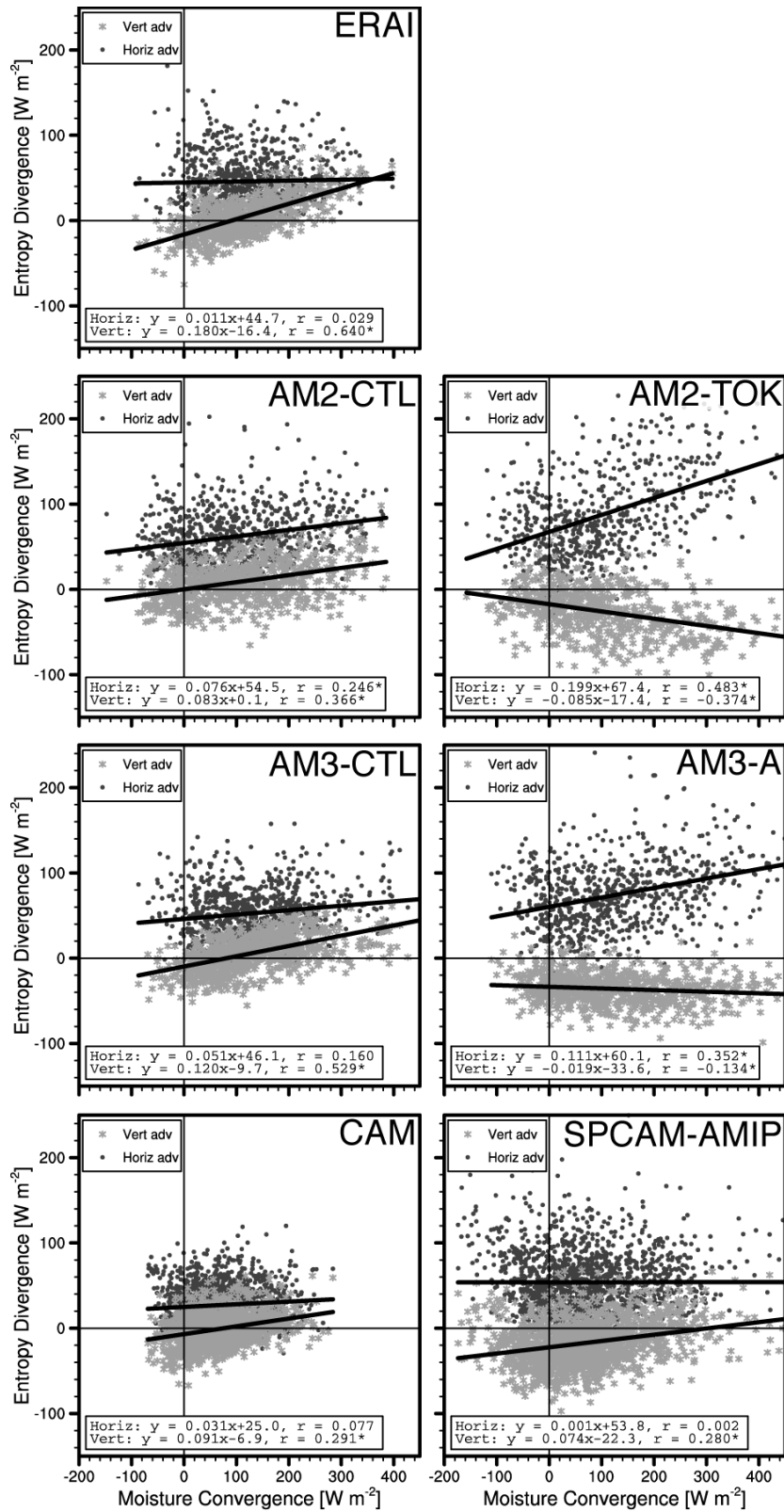
○ AM2-CTL □ AM3-CTL △ CAM
 ● AM2-TOK ■ AM3-A ▲ SPCAM-AMIP

961

962

963 **Figure 6.** The relationship between October-April mean Γ_V and one metric of the robustness of MJO
 964 eastward propagation. Spatial averaging to include only oceanic points within the climatological
 965 convective region (see text) has been applied to Γ_V . The MJO metric is the ratio of eastward to
 966 westward tropical rainfall power within the MJO spectral region [periods 30-96 days, zonal
 967 wavenumbers +1 to +3 (eastward) or -1 to -3 (westward)]. Also shown are the best-fit line equation
 968 and correlation coefficient r .

969

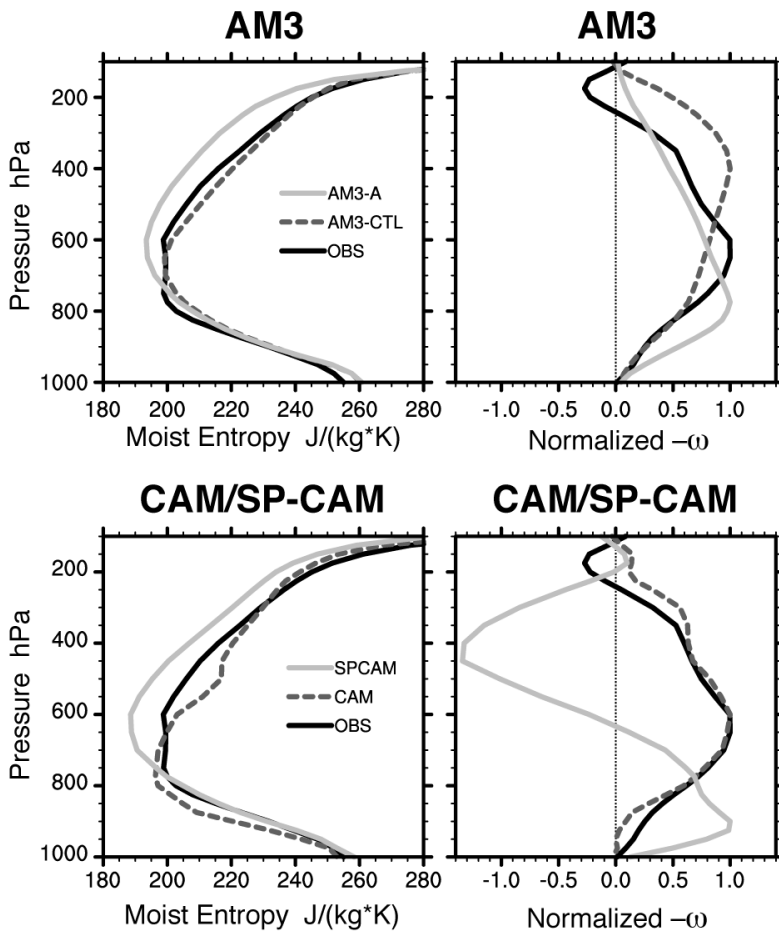


970

971

972 **Figure 7.** Horizontal (dark bullets) and vertical (light stars) advective components of vertically
973 integrated moist entropy divergence versus VIMC averaged over the east Indian Ocean region (70°-
974 100°E, 10°S-5°N) during October-April. Conditional sampling has been done to include only times
975 when the 91-day windowed variance of a precipitation index (i.e., rainfall averaged over the east Indian
976 Ocean region and then 20-100-day filtered) is greater than its winter average value. Land points are
977 omitted from the spatial averages. Each point represents a single day. Thick black best-fit lines are
978 overlaid, and the corresponding equations and correlation coefficients r appear at the bottom of each
979 panel. Starred r values are statistically significant above the 95% confidence level.

980

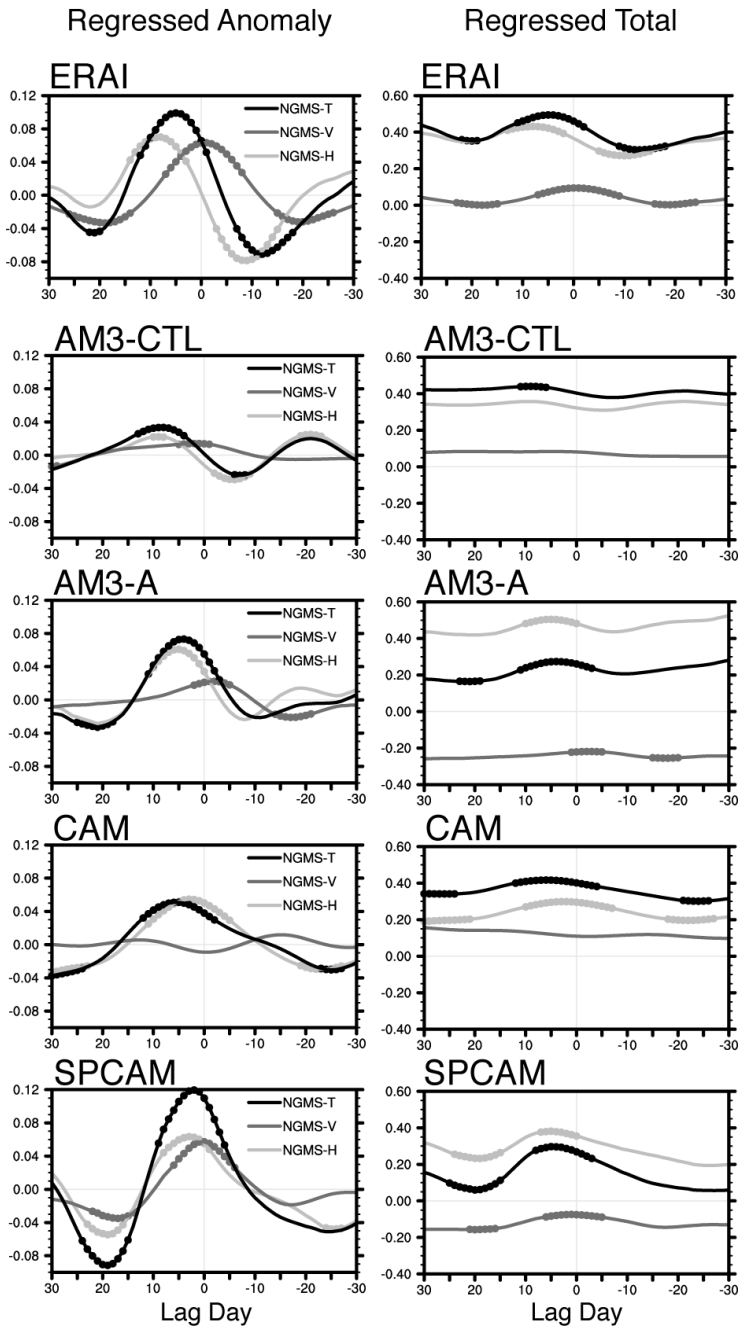


981

982

983 **Figure 8.** MJO suppressed-phase profiles of (left) moist entropy s and (right) pressure velocity $-\omega$
 984 normalized by the value of peak upward motion for (top) AM3 and (bottom) CAM/SPCAM simulations.
 985 Profiles are conditionally averaged over the equatorial east Indian Ocean (85° - 95°) to include only those
 986 days between October and April in which a MJO rainfall index is less than -1σ . We use 20-100-day
 987 filtered and standardized east Indian Ocean rainfall as our index.

988



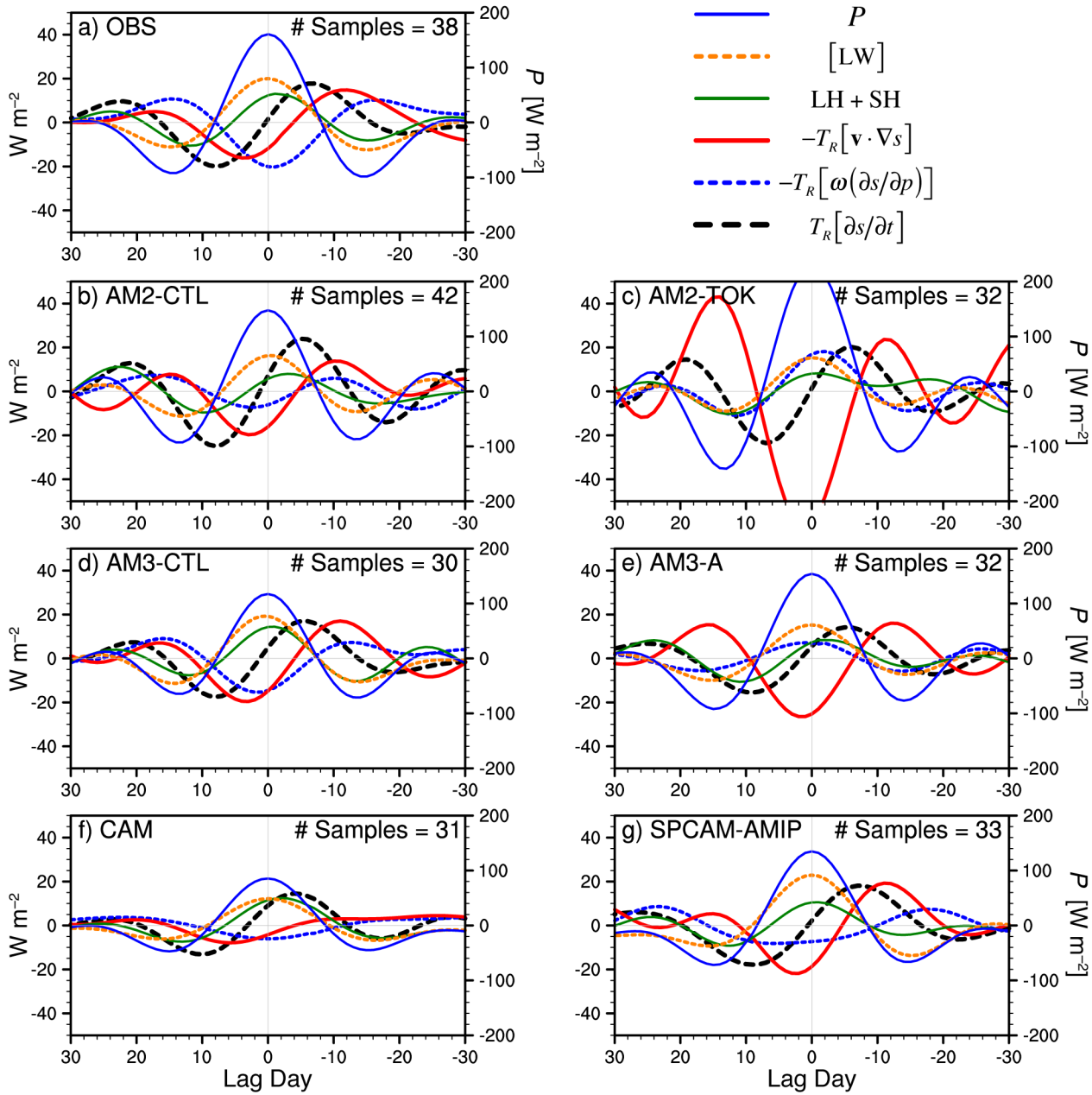
989

990

991 **Figure 9.** (left) Anomalous and (right) total NGMS linearly regressed onto a MJO precipitation index at
 992 90°E. Regression time series index is defined as 20-100-day filtered (“MJO-filtered”) and standardized
 993 precipitation averaged between 10°S-10°N at 90°E. Each plot shows the total (NGMS-T, or Γ_T ; black),
 994 vertical (NGMS-V, or Γ_V ; dark gray), and horizontal (NGMS-H, or Γ_H ; light gray) components of

995 NGMS. Regressed variables have been averaged to include only those latitudes where climatological
996 VIMC is positive (see text). For anomaly plots, variables are MJO-filtered departures from the
997 calendar-day mean. Dotted line sections denote values that are statistically significant above the 92.5%
998 level. Lag days appear along x-axis, and negative lag days occur before maxima in the MJO rainfall
999 index.

1000



1001
 1002
 1003
 1004
 1005
 1006
 1007

Figure 10. Budget of equatorial (15°S-10°N) moist entropy based on a composite of winter (Sep-Apr) MJO events in the east Indian Ocean for (a) ERAI/TRMM and (b-g) GCM simulations. All variables are 20-100-day filtered and are shown in energy units ($W m^{-2}$). MJO events are defined as local maxima that exceed $+1\sigma$ in a MJO-filtered and standardized east Indian Ocean precipitation index. Left y-axis scale is for terms contributing to the moist entropy budget and the right y-axis scale is for

1008 precipitation P (solid blue line in each panel). Lag days are at the bottom of each panel, with negative
1009 days occurring before the MJO peak rainfall. Composite sample sizes appear at the upper right of each
1010 panel. Square brackets represent vertical integrals from the surface to 100 hPa. Vertically integrated
1011 shortwave heating is negligible and is omitted.